Homochiral versus Racemic 2D Covalent Organic Frameworks

José del Refugio Monroy,[1,2] Joël Schlecht,[1] Clara Douglas,[2] Robbie Stirling,[1] Glen J. Smales,[3] Zdravko Kochovski,[4] and Oliver Dumele[2,5,6]*

1) Department of Chemistry & Center for the Science of Materials Berlin, Humboldt-Universität zu Berlin, Brook-Taylor-Strasse 2, 12489 Berlin, Germany.

2) Department of Organic Chemistry, Albert-Ludwigs-Universität Freiburg, Albertstrasse 21, 79104 Freiburg, Germany.

3) Bundesanstalt für Materialforschung und prüfung, Unter den Eichen 87, 12205 Berlin, Germany.

4) Department for Electrochemical Energy Storage, Helmholtz-Zentrum Berlin für Materialien und Energie, Hahn-Meitner-Platz 1, 14109 Berlin, Germany.

5) Freiburg Materials Research Center, Albert-Ludwigs-Universität Freiburg, Stefan-Meier-Strasse 21, 79104 Freiburg, Germany

6) Freiburg Center for Interactive Materials and Bioinspired Technologies, Albert-Ludwigs-Universität Freiburg, Georges-Köhler-Allee 105, 79110 Freiburg, Germany

Chirality, Chiral Materials, [n]Helicenes, Covalent Organic Frameworks, Liebisch–Wallach's rule

ABSTRACT: The synthesis of homochiral two-dimensional Covalent Organic Frameworks (2D COFs) from chiral π-conjugated building blocks is challenging, as chiral units often lead to misaligned stacking interactions. In this work, we introduce helical chirality into 2D COFs using configurationally stable enantiopure and racemic [5]helicenes as linkers in the backbone of 2D **[5]HeliCOFs**. Through condensation with 1,3,5-triformylbenzene (TFB) or 1,3,5-triformylphloroglucinol (TFP), our approach enables the efficient formation of a set of homochiral and racemic 2D **[5]HeliCOFs**. The resulting carbon-based crystalline and porous frameworks exhibit distinct structural features and different properties between homochiral and their racemic counterparts. Propagation of helical chirality into the backbone of the crystalline frameworks leads to the observation of extended chiroptical properties in the far-red visible spectrum, along with a less compact structure compared to the racemic frameworks. The present study offers insight into general chiral framework formation and extends the Liebisch–Wallach rule to 2D COFs.

Introduction.

Carbon-based homochiral architectures with complex structural features can establish unique connections between molecular and global chirality.[1-6] The amplified chiroptical properties of such all-carbon structures usually are linked to their dimensionality — being either discrete molecules,[7-11] macromolecules,[12-18] or supramolecular assemblies.[19-24] For example, organic homochiral polymers frequently show amplified chiroptical properties compared to their unichiral building blocks, as their resulting interconnected asymmetric networks exhibit a new set of photophysical and electronic properties.[25-28] Hence, all-organic homochiral structures, derived from precisely designed enantiopure organic units, offer the opportunity to be explored in fundamental research and functional materials.

Conceptually, reticular chemistry allows the incorporation of chiral organic building blocks across highly periodic frameworks, integrating their initial chiral information into novel salient functionalities of infinite homochiral structures.[29-31] In particular, Covalent Organic Frameworks (COFs) are an interesting example of highly ordered and porous solids with fine-tunable carbon-based structures.[32, 33] Until now, introducing enantiopure all-carbon building blocks into two-dimensional (2D) COFs has remained as a synthetic challenge, as the intrinsic non-planarity of the chiral units could cause a significant deviation in the stacking of crystalline lattices.[34-36] For instance, the first example of 2D chiral COFs was obtained by post-synthetic side-chain modification from planar building blocks to avoid the presumed steric mismatch in the backbone of the 2D lattices(Figure 1a).[37] Subsequently, various approaches have been developed to incorporate or induce chirality into 2D COFs, including chiral-preorganized building blocks,[38-42] metal-template synthesis,[43-47] enrichment with enantiopure biomolecules,[48,49] and using enantiopure modulators.[50-52] Such advanced 2D homochiral COFs are mainly studied in chiral separation technology,[53,54] enantioselective catalysis,[55-57] light-emissive materials,[58-60] chiroptical nanoarchitectonics,[61, 62] and fundamental studies[63] — such as, the formation of metal-helical rods.[47]

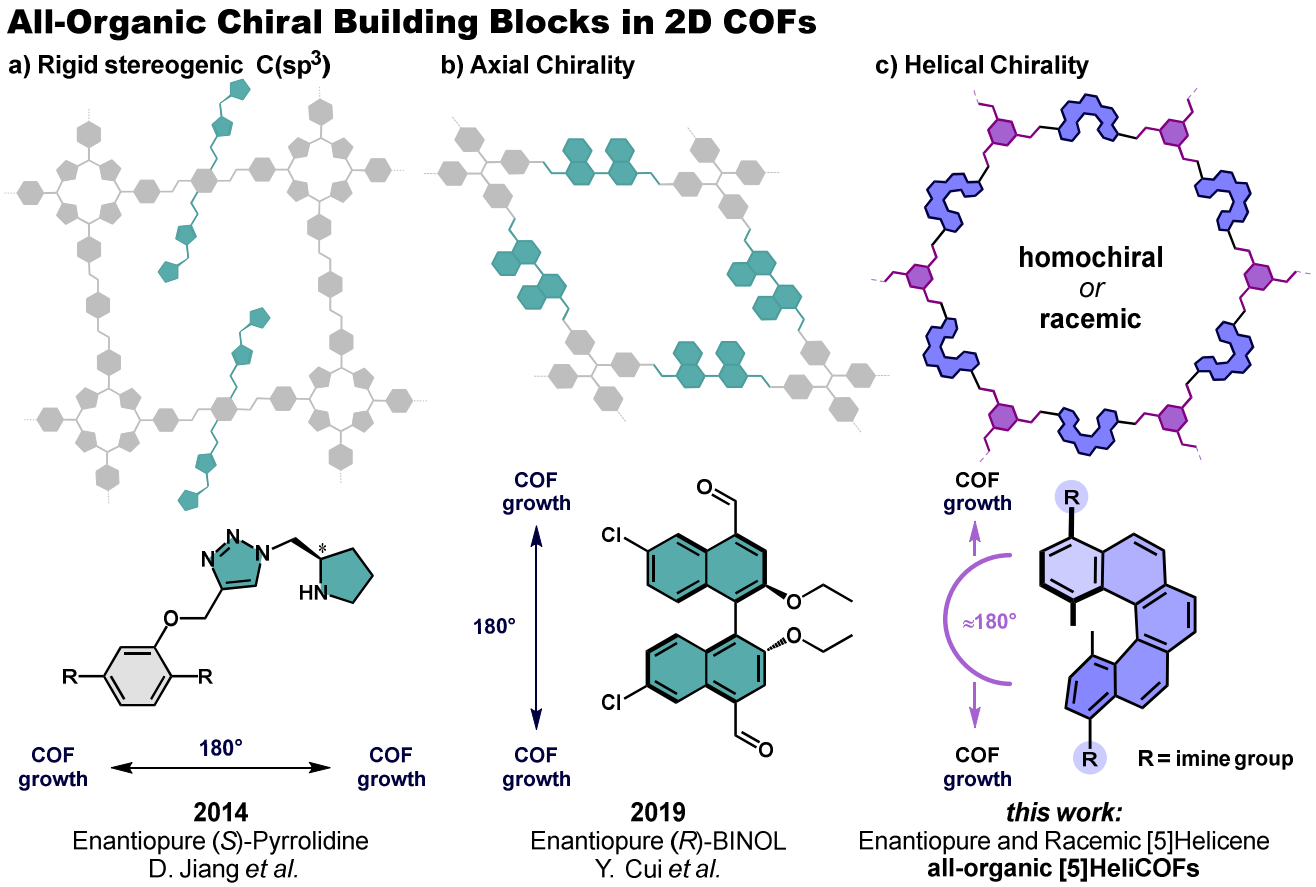

Figure 1. Representative examples of previously reported carbon-based chiral building blocks for the synthesis of 2D chiral COFs; (a) homochiral 2D COFs bearing the C(sp^3) stereocenter in the side chain;[37] (b) incorporation of axial chirality in the backbone of 2D homochiral COFs from (*R*)-BINOL based building blocks;[72] (c) in this work: incorporation of helical chirality into the back-bone of 2D COFs with configurationally stable [5]helicenes as *pseudo*-C_2 linear linkers for the synthesis of all-organic 2D **[5]HeliCOFs**.

Currently, carbon-based non-planar building blocks have been incorporated into the backbone of 2D COFs,[64] contributing in the development of complex carbon-based architectures, which no longer rely on planar stacking units.[65-71] Establishing non-planar 2D COFs have inspired the incorporation of complex chiral geometries into these novel π-conjugated frameworks, leading to homochiral architectures with extended chiral information derived from their inherently curved π-system in the organic backbone. For example, axial chirality has been incorporated into the backbone of homochiral 2D COFs with a precisely designed enantiopure (*R*)-BINOL derivative as a *pseudo*-C_2 linker (Figure 1b), pioneered by Cui and co-workers.[72] However, homochiral 2D COFs are rarely synthesized using enantiopure carbon-based π-conjugated building blocks due to their challenging multistep synthesis.[73-76]

Alongside that, despite the growing interest in homochiral 2D COFs, reports on two opposite homochiral lattices versus their racemic analogue are rare.[47, 58, 59] Systematic studies on these fundamental structural differences could help to derive general trends from the influence of the absolute configuration of the building blocks on the formation of homochiral (or racemic) 2D frameworks. Inherently, a high degree of crystallinity is an essential property of COFs.[77,78] As an analogy to Liebisch–Wallach's rule,[79, 80] which states that racemic single crystals are more densely pack and usually preferred over their homochiral counterparts,[81, 82] racemic building blocks should lead to 2D COFs with higher density than their homochiral versions. Following this rule, racemic 2D COFs should also possess a higher degree of crystallinity than their homochiral analogues, due to preferred stacking interactions based on the complementary geometries from their racemic units. However, the structural analogy of Liebisch–Wallach's rule to the growth of homochiral versus racemic lattices has not been experimentally studied in all-organic 2D framework materials.[83] As a result of this fundamental comparison,[84-91] it would be possible to discover general structural tendencies that eventually lead to rationally designed homochiral (or racemic) 2D COF architectures with unique topologies and large chiroptical activity, revealing further potential applications of these novel materials.

In this context, [*n*]helicenes[92, 93] have led to intensive investigation of their photophysical and electronic properties, drawing attention to their incorporation into complex carbon-based unichiral architectures,[94-102] homochiral organic polymers,[103-105] and non-covalent assemblies.[106-108] Hence, incorporating enantiopure [*n*]helicenes into the backbone of 2D COFs could reveal fundamental structural differences in homochiral versus racemic 2D extended lattices. Racemic [6]- and [7]helicenes have been used as building blocks in 2D COFs.[70, 71] However, enantiopure [*n*]helicenes have not yet been incorporated into

homochiral 2D COFs, and their intrinsic helical chirality remains unexplored in crystalline and porous all-organic solids. Currently, there is no systematic report on the structural preferences derived from homochiral versus racemic 2D COFs using chiral π-conjugated building blocks.

In this work, we introduce carbon-based helical chirality into the backbone of imine-linked homochiral (and racemic) 2D COFs by using enantiopure (or racemic) configurationally stable [5]helicene derivatives as *pseudo*-C_2 linkers for the synthesis of all-organic 2D **[5]HeliCOFs** (Figure 1c). We evaluated systematically the influence of their absolute structural configuration under identical experimental conditions on the formation of homochiral and racemic 2D **[5]HeliCOFs** which displayed remarkable crystalline, porous, and extended chiroptical properties.

Results and discussion.

Design and synthesis of [5]helicene building blocks. We identified that 4,11-substituted [5]helicenes could be tested as *pseudo*-C_2 linkers for the synthesis of homochiral (or racemic) 2D COFs (Figure 1c). This substitution pattern offers a nearly 180° angle required for a formal C_2 linker to be incorporated into the backbone of extended 2D lattices, while also exhibiting a non-planar geometry, enabling the incorporation of carbon-based helical chiral into the backbone of the homochiral 2D frameworks. Commonly, enantiopure [5]helicene racemizes in solution at 25 °C.[109-111] To avoid its epimerization, methyl substituents were introduced at the 1,14-positions of the [5]helicene core, following the synthetic approach developed by *Juříček* and co-workers.[112] This precise modification allows that enantiopure [5]helicene building blocks retain their initial absolute configuration during the standard 2D COFs synthesis (ca. 120 °C).

At first, the racemic [5]helicene core, (±)-4,11-dibromo-1,14-dimethyl[5]helicene ((±)-**1**) was synthesized on enlarged scale following a photocyclodehydrogenation reaction based on previously reported procedures (SI, Section S2).[112, 113] The bromine atoms in the 4- and 11-positions of (±)-**1** allow the incorporation of diverse substituents for the synthesis of 2D **[5]HeliCOFs**. For instance, *N*–aryl benzophenone imines have proven to be effective moieties for the synthesis of highly crystalline and porous imine-linked 2D COFs.[114, 115] In addition, benzophenone imine-based building blocks tend to be more stable to oxidation on air than their free amine version.[116-118] Thus, we aimed for the incorporation of *N*–aryl benzophenone imine groups with an additional phenyl ring, to extend the racemic [5]helicene core (±)-**1**. This was achieved using Suzuki–Miyaura cross-coupling with boronic ester **2** to obtain (±)-**3** in excellent yields (90%, Scheme 1).[119] After the acidic hydrolysis of the benzophenone imine groups, the unambiguous structural proof of the racemic diamine (±)-**3b** was obtained by single-crystal X-ray analysis, exhibiting 21° deviation from a formal C_2 linker, induced by the helical nature of (±)-**3b** (Figure S76).

Aside from that, an alternative synthetic route was established to obtain the enantiopure building blocks (*P*)- and (*M*)-**3** (Scheme 1). In this case, the enantiopure boronate auxiliary (*R*,*R*)-bis(hydrobenzoinato)diboron ((*R*,*R*)-**4**) was coupled to the parent racemic [5]helicene core (±)-**1** in a Miyaura borylation to obtain the mixture of diastereomers (*R*,*R*)-(*P*/*M*)-**5** in good yield (87%, Scheme 1).[120] Next, the diastereomeric

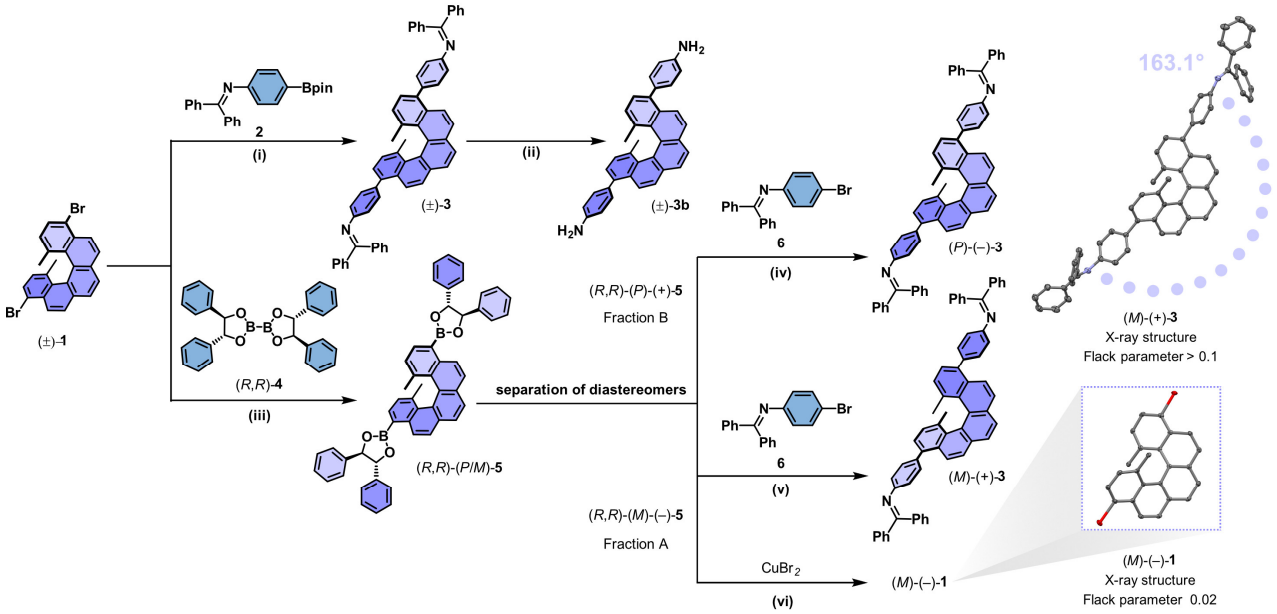

Scheme 1. Synthesis of racemic and enantiopure [5]helicene building blocks. Reagents and conditions: (i) **2**, $Pd(PPh_3)_4$, Cs_2CO_3, DMF/water 4:1, 110 °C, 16 h, 90%; (ii) aq. AcOH (6 M), 1,4-dioxane, 70 °C, 2 h, 80%; (iii) (*R*,*R*)-(+)-**4**, [$Pd(dppf)Cl_2 \cdot CH_2Cl_2$], CH_3COOK, 1,4-dioxane, 80 °C, 45 min, 87%; (iv) (*R*,*R*)-(*P*)-(+)-**5**, **6**, $Pd(PPh_3)_4$, Cs_2CO_3, DMF/water 4:1, 110 °C, 20 h, 68%; (v) (*R*,*R*)-(*M*)-(−)-**5**, **6**, $Pd(PPh_3)_4$, Cs_2CO_3, DMF/water 4:1, 110 °C, 20 h, 75%; (vi) (*R*,*R*)-(*M*)-(−)-**5**, $CuBr_2$, methanol/water 4:1, 85 °C, 12 h, 98%; (inset) single-crystal X-ray structure of (*M*)-(+)-**3** or (*P*)-(−)-**3** with a Flack parameter > 0.1 (angle measured along atoms N–C_{Ph}—N), and single-crystal X-ray structure of the enantiopure (*M*)-(−)-**1** with a Flack parameter 0.02 (hydrogen atoms are omitted for clarity).

mixture (*R*,*R*)-(*P*/*M*)-**5** was resolved using preparative high-performance liquid chromatography with a Pirkle-type chiral stationary phase (Figure S64).[121] Subsequently, the diastereomers (*R*,*R*)-(*P*)-(+)-**5** (fraction B, *ee* = 99.6%), and (*R*,*R*)-(*M*)-(−)-**5** (fraction A, *ee* = 99.9%), were subjected to cross-coupling reaction with **6**, readily losing the chiral auxiliary and leading to the enantiopure *N*-benzophenone diimines (*P*)-(−)-**3** and (*M*)-(+)-**3** in adequate yields (68% and 75%, respectively, Scheme 1). Single-crystals suitable for X-ray analysis were obtained for (*M*)-(+)-**3**. However, we faced theoretical limitations in directly assigning the absolute configuration from the measured crystals with high accuracy, due to weak resonant scattering caused by the absence of heavy atoms in the enantiopure (*M*)-(+)-**3** (Figure S77).[122,123] Nevertheless, the X-ray analysis provided the structure of the [5]helicene building block with *N*-benzophenone imine moieties (Scheme 1), exhibiting 16.9° deviation from a formal linear COF linker due to its helical nature. To determine the absolute configuration, the isolated diastereomer (*R*,*R*)-(*M*)-(−)-**5** (fraction A) was subjected to a direct bromodeboronation to obtain the enantiopure dibromo[5]helicene (*M*)-(−)-**1** in excellent yields (98%, Scheme 1, bottom).[124] With these bromine atoms, it was possible to assign the absolute configuration of (*M*)-(–)-**1** from the single-crystal X-ray analysis with high accuracy (Table S15). Thus, all subsequent [5]helicene derivatives synthesized from the isolated diastereomer (*R*,*R*)-(*M*)-(−)-**5** (fraction A) hold an (*M*)-configuration. Additionally, the absolute configuration of the enantiopure [5]helicene building blocks was validated using a combination of electronic circular dichroism (ECD) spectroscopy, optical rotatory dispersion, and time-dependent density functional theory (TD-DFT) calculations (Figures S67–68).[125] Hence, our strategy enables rapid access to enantiomerically pure and racemic [5]helicenes in sufficient quantities for studying comparative synthesis of homochiral and racemic 2D COFs.

Synthesis of racemic [5]HeliCOFs. The formation of racemic **[5]HeliCOFs** using the racemic *pseudo*-linear linker (±)-**3** was first investigated due to its direct synthetic accessibility. We chose 1,3,5-triformylbenzene (TFB) and 1,3,5-triformylphloroglucinol (TFP) as nodes (Scheme 2). In brief, *rac*-**[5]Heli-TFB** COF was synthesized under acidic solvothermal conditions with 21 equiv. of aq. AcOH (6 M) using *o*-DCB/*n*-BuOH 1:1 as a solvent mixture at 120 °C for 72 h, with a yield of 69% (for experimental screening of reaction conditions, see Table S1). The formation of a highly crystalline solid was confirmed by powder X-ray diffraction (PXRD) of *rac*-**[5]Heli-TFB** COF (Figure 2a), where narrow and intense reflexes at low 2θ angles can be observed. There, *rac*-**[5]Heli-TFB** COF exhibits an intense reflex at $2\theta = 2.4°$, assigned to the (100) facet, and lower intense reflexes at 4.7° and 7.2°, which correspond to the (200) and (120) planes, in agreement with the simulated diffraction pattern of a hexagonal AA-inclined stacking mode (Figure S51).[126] The Pawley refinement provided a good agreement with the hexagonal proposed model (refined lattice parameters $a = b = 45.7$ Å and $c = 7.4$ Å, with *P*1 as space group) (Figure S50). In the proposed hexagonal AA-inclined model, the (*P*)- and (*M*)-[5]helicene cores are arranged on top of each other, alternating their *fjord*-region over the racemic 2D lattices (Figure S51). This alternating pair-packing of complementary enantiomers has been observed in racemic [*5*]helicene single crystals,[127,128] and *rac*-[*n*]helicene COFS ($n > 6$)[70, 71] suggesting that the racemic *pseudo*-linear linker (±)-**3** have been successfully incorporated into the extended crystalline frameworks. Furthermore, the periodic lattices of *rac*-**[5]Heli-TFB** COF were directly visualized using low-dose cryogenic high-resolution transmission electron microscopy (HR-TEM) (Figure 2b), where hexagonal domains can be observed along the [001] plane. In addition, the corresponding fast Fourier transform (FFT) pattern of the HR-TEM image, supports a hexagonal symmetry with a *d*-spacing of 4.08 nm (Figure 2b). Thus, the direct visualization of honeycomb-type 2D lattices is in agreement with the experimental PXRD diffractogram, and supports the proposed

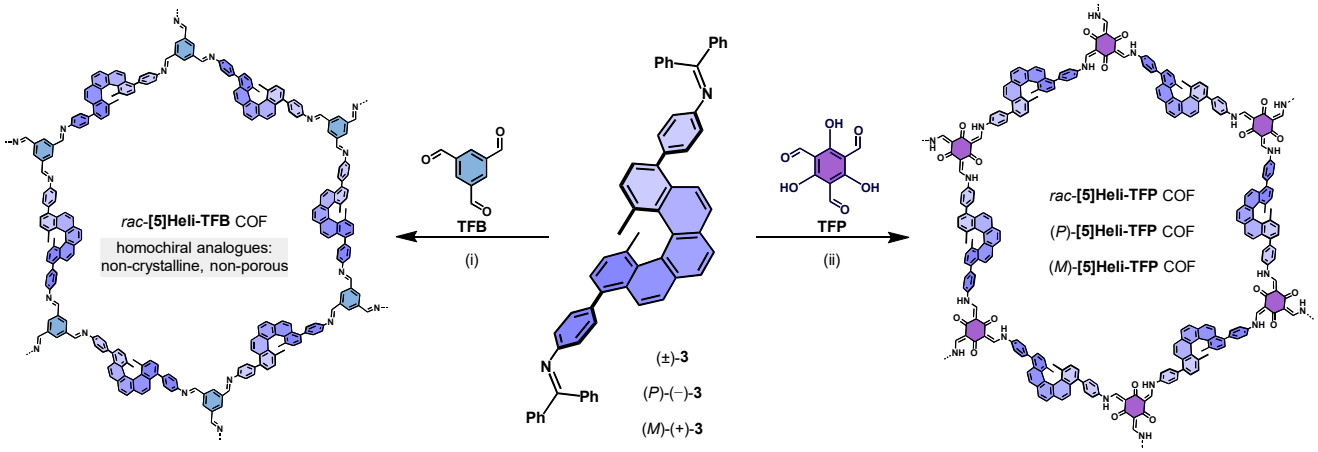

Scheme 2. Acidic solvothermal synthesis of racemic and homochiral 2D **[5]HeliCOFs** based on 1,3,5-triformylbenzene (TFB) and 1,3,5-triformylphloroglucinol (TFP) as nodes and testing (±)-**3**, (*P*)-(−)-**3** and (*M*)-(+)-**3** as *pseudo*-C_2 linkers; reagents and experimental conditions: (i) TFB, aq. AcOH (6 M, 21 equiv.), *o*-DCB/*n*-BuOH 1:1, 120 °C, 72 h, 69% *rac*-**[5]Heli-TFB** COF (homochiral analogues were not obtained under identical experimental conditions); (ii) TFP, aq. AcOH (6 M, 40 equiv.), aniline (0.7 M, 1.5 equiv.), *o*-DCB/*n*-BuOH 4:1, 120 °C, 72 h, 96% *rac*-**[5]Heli-TFP** COF, 96% (*P*)-**[5]Heli-TFP** COF and 90% (*M*)-**[5]Heli-TFP** COF.

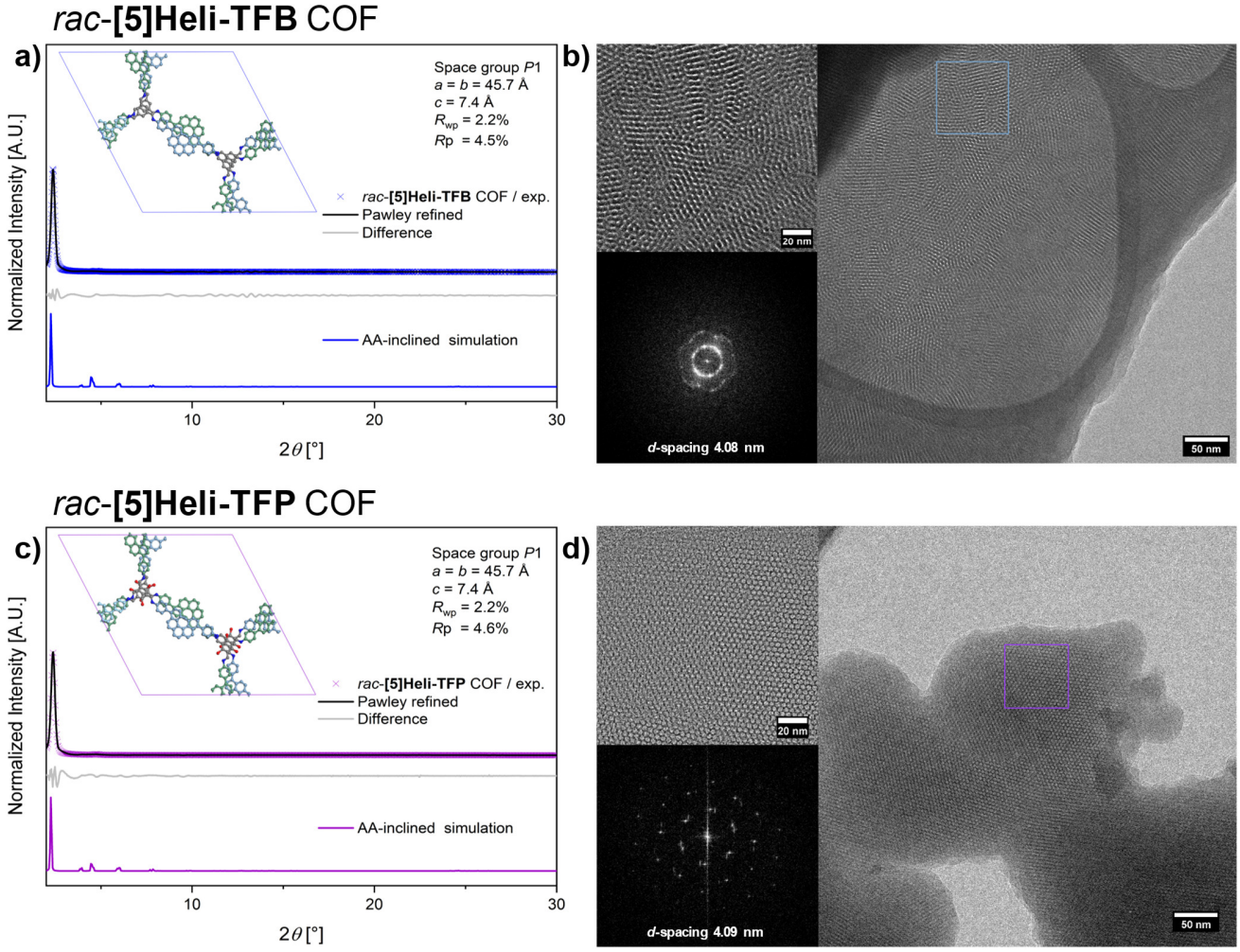

Figure 2. Characterization of *rac*-**[5]Heli-TFB** COF and *rac*-**[5]Heli-TFP** COF; (a) experimental (blue crosses), simulated PXRD patterns (blue line), Pawley refinement (black line) using AA-inclined stacking model, difference between Pawley refinement and AA-inclined simulation (gray) of *rac*-**[5]Heli-TFB** COF; (b) low-dose cryo-HR-TEM of *rac*-**[5]Heli-TFB** COF, inset: expansion of the blue square region showing hexagonal features along the [100] direction, and FFT of the region indicated; (c) experimental (purple crosses), simulated PXRD patterns (purple line), Pawley refinement using AA-stacking model (black line), difference between Pawley refinement and AA-inclined simulation (gray) of *rac*-**[5]Heli-TFP** COF; (d) low-dose cryo-HR-TEM of *rac*-**[5]Heli-TFP** COF, inset: expansion of the purple square region showing hexagonal features along the [100] direction, and FFT of the region indicated.

highly symmetric hexagonal structural model with an AA-inclined stacking mode. Subsequently, the porosity of *rac*-**[5]Heli-TFB** COF was investigated using isothermal N_2-sorption measurements at 77 K (Figure S23). The adsorption data show two inflection points below p/p_0 = 0.2, associated with mesoporous materials according to a type IV isotherm.[129] Furthermore, the surface area was calculated using the Brunauer–Emmett–Teller (BET) method, showing a porosity value of 504 $m^2 g^{-1}$.[130] Also, the pore size distribution has been estimated using nonlinear density functional theory (NL-DFT) with a maximum of around 36 Å (Figure S27). Next, the morphology of *rac*-**[5]Heli-TFB** COF was observed in the FE-SEM micrographs (Figure S39), showing spherical-shaped particles with diverse diameters from ca. 1.8 to 8.8 µm. Furthermore, its thermal stability was confirmed up to 350 °C by thermogravimetric (TGA) analysis (Figure S43). Additionally, the chemical composition of *rac*-**[5]Heli-TFB** COF was analyzed. For example, the Fourier-transform infrared (FTIR) spectrum presents the C=N stretch band at 1595 cm^{-1}, and the absence of the C=O stretch band of TFB at 1695 cm^{-1}, indicating the formation of imine-linkages (Figure S46). Which it is also supported by the ^{13}C cross-polarization magic-angle spinning nuclear magnetic resonance (CP-MAS NMR) spectrum showing a signal at 156.6 ppm associated to the C=N imine linkage (Figure S48). Our findings indicate that *rac*-**[5]Heli-TFB** COF is a highly crystalline organic solid with 2D honeycomb architecture and mesoporous structure.

With the complete analysis of *rac*-**[5]Heli-TFB** COF and optimized reaction conditions in hand. We aimed for test the enantiopure building blocks (*P*)-(–)-**3** and (*M*)-(+)-**3** as *pseudo*-C_2 linkers with TFB as a node to explore the formation of homochiral (*P*)- or (*M*)-**[5]Heli-TFB** COFs, using identical experimental conditions. Despite rigorous repetitions, our attempts to obtain the homochiral version of *rac*-**[5]Heli-TFB** COF remained unsuccessful, yielding amorphous and non-porous solids (Figure S21). Possibly, the enantiopure [5]helicenes induce too large deviations of the lattices, preventing the formation of crystalline packing motifs to grow homochiral 2D lattices. These unexpected results highlight the complexity of the

synthesis of homochiral 2D COFs using carbon-based π-conjugated building blocks.

Hence, we turned to TFP as a node for the synthesis of *rac*-**[5]Heli-TFP** COF, testing (±)-**3** as a linker (Scheme 2). From using TFP, we anticipated that β-ketoamine linkages could stabilize the homochiral crystallization of **[5]HeliCOF** based on enantiopure *pseudo*-C_2 linkers.[131, 132] Additionally, a modulation strategy based on the addition of aniline was applied.[133] In this case, *rac*-**[5]Heli-TFP** COF was obtained under acidic solvothermal conditions with 40 equiv. aq. AcOH (6 M), 1.5 equiv. aniline, *o*-DCB/*n*-BuOH 4:1 as solvent at 120 °C for 72 h with a high yield (96%, for the synthetic screening conditions see Table S2). Notably, the experimental PXRD pattern of *rac*-**[5]Heli-TFP** COF exhibits narrow reflexes at low 2θ angles at 2.5°, attributed to the (100) facet, and less intense reflexes at 4.2° and 8.5°, corresponding to the (200) and (120) planes, respectively (as shown in Figure 2c). The simulated diffraction pattern of the hexagonal AA-inclined stacking model agrees with the experimental PXRD diffractogram, and Pawley refinement provided a good agreement with our proposed hexagonal AA-inclined stacking model (refined lattice parameters $a = b = 45.7$ Å and $c = 7.4$ Å, with *P*1 as space group, Figure S54).[126] Similarly to *rac*-**[5]Heli-TFB** COF, we propose a symmetric hexagonal structural model in which (*P*)- and (*M*)-[5]helicene are alternately stacked on top of each other over the 2D lattices (Figure 4a). In addition, low-dose HR-TEM of *rac*-**[5]Heli-TFP** COF reveals honeycomb-type lattices (Figure 2d), with a *d*-spacing of 4.09 nm, and FFT pattern showing a honeycomb-type phase projected along the (100) axis. These representative images are consistent with the PXRD analysis, indicating the presence of structural hexagonal AA-inclined 2D crystalline lattices for *rac*-**[5]Heli-TFP** COF. Furthermore, N_2-sorption measurements at 77 K of *rac*-**[5]Heli-TFP** COF show two inflection points below $p/p_0 = 0.2$ (Figure 3b), associated with mesoporous solids according to a type IV isotherm,[129] with a significant BET surface area of 782 $m^2 g^{-1}$ (Figure S24).[130] The pore size distribution has been estimated using NL-DFT with a maximum of around 35.3 Å (Figure S28). Also, thermal stability was confirmed up to 350 °C by TGA analysis (Figure S43). Furthermore, FTIR spectroscopy shows the characteristic C═O stretch band at 1582 cm^{-1} and C-N stretch band at 1285 cm^{-1} indicating the presence of ketoenamine linkages (Figure S47), in agreement with the CP-MAS NMR spectrum showing a peak at 185.2 ppm corresponding to ketone carbon (Figure S49). Our results indicate that *rac*-**[5]Heli-TFP** COF is a highly crystalline and porous organic solid with an 2D symmetric hexagonal lattices.

Synthesis of homochiral 2D [5]HeliCOFs. The enantiopure building blocks (*P*)-(–)-**3** and (*M*)-(+)-**3** were tested as *pseudo*-C_2 linkers in combination with TFP as a node, using identical experimental conditions previously optimized for *rac*-**[5]Heli-TFB** COF to obtain the homochiral analogues (*P*)-**[5]Heli-TFP** COF and (*M*)-**[5]Heli-TFP** COF (Scheme 2). Interestingly, the experimental PXRD diffractograms of *rac*-**[5]Heli-TFP** COF, and homochiral (*P*)- and (*M*)-**[5]Heli-TFP** COFs display similar angular positions of Bragg reflexes, but their relative intensities are clearly distinct from each other. In particular, the PXRD patterns of the homochiral samples display a intense reflex at $2\theta = 4.2°$, corresponding to the (200) facet (Figure 3a). In contrast, the racemic sample shows a significantly more intense reflex at $2\theta = 2.5°$, attributed to the (100) facet (Figure 3a). These differences suggest higher structural offset between the crystalline lattices in the homochiral analogues.[134-136] Consequently, we propose that homochiral (*P*)- and (*M*)-**[5]Heli-TFP** COFs predominantly adopt an asymmetric hexagonal structure, characterized by an equal statistical

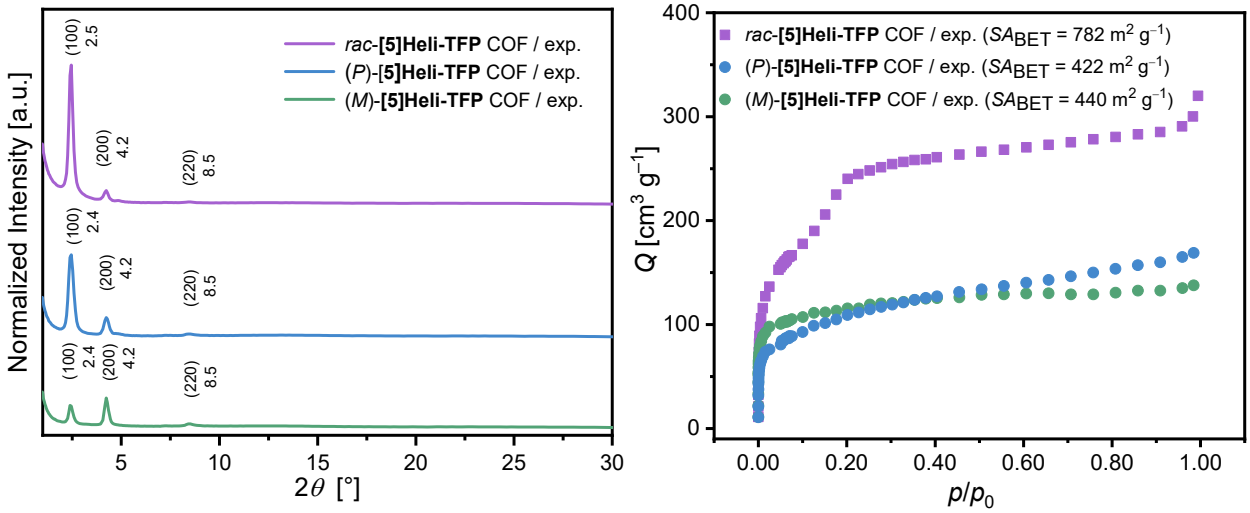

Figure 3. Properties of homochiral and racemic **[5]Heli-TFP** COFs; (left) experimental PXRD diffractograms of *rac*-**[5]Heli-TFP** COF (purple line), (*P*)-**[5]Heli-TFP** COF (blue line), and (*M*)-**[5]Heli-TFP** COF (green line); (right) N_2 adsorption isotherms at 77 K of *rac*-**[5]Heli-TFP** COF (purple squares), (*P*)-**[5]Heli-TFP** COF (blue dots) and (*M*)-**[5]Heli-TFP** COF (green dots).

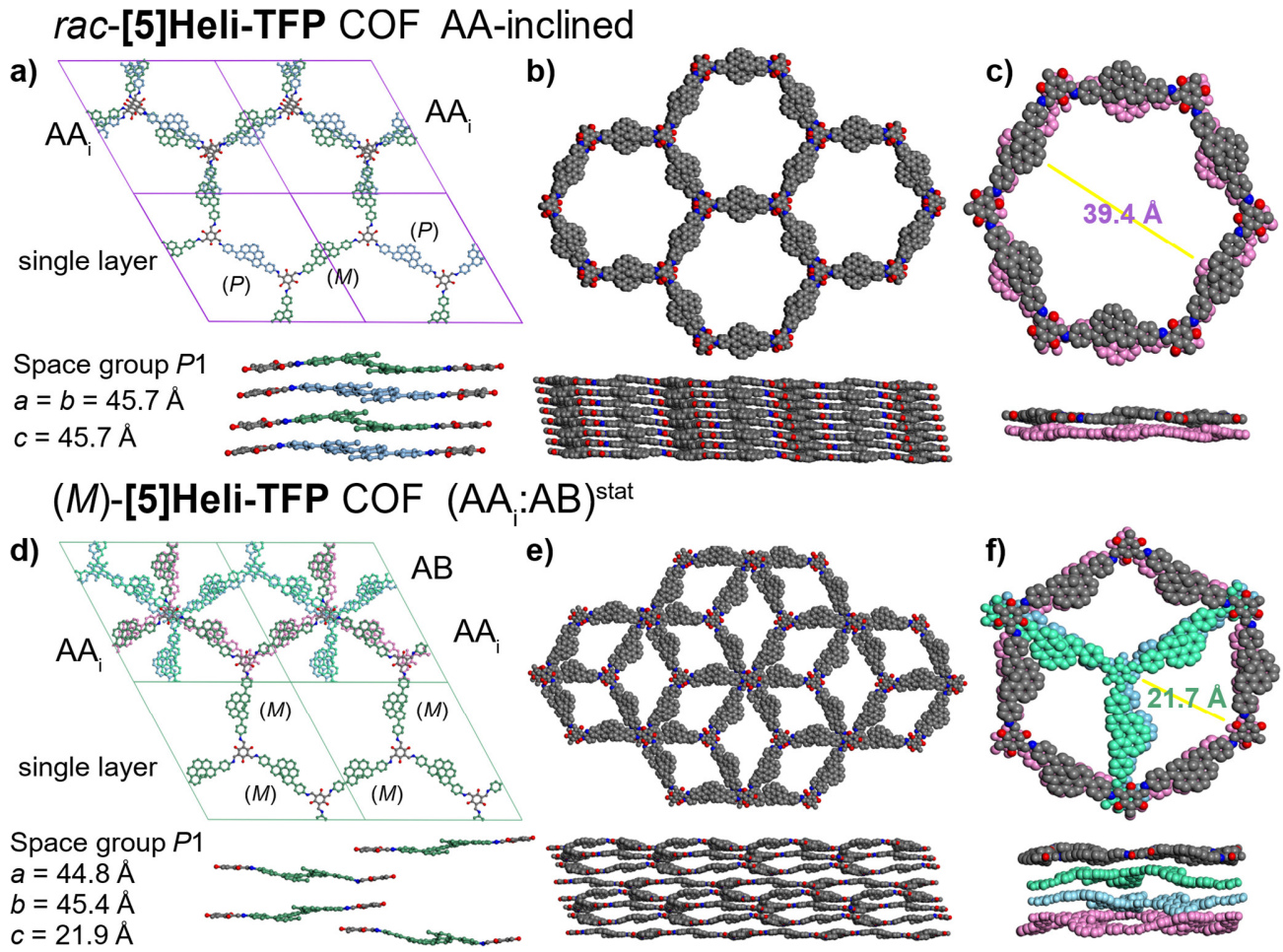

Figure 4. Proposed structural representations of racemic and homochiral **[5]Heli-TFP** COFs. (a) Pawley-refined structural model of *rac*-**[5]Heli-TFP** COF with AA-inclined stacking mode (top: complete unit cells, bottom: single layer); (b) top and side view on the corresponding refined structure; (c) example of single hexagonal pore as double-layer extracted from the refined model. (d) Pawley refinement asymmetric structural model of (*M*)-**[5]Heli-TFP** COF with multilayer statistical representation $(AA_i:AB)^{stat}$, illustrating the asymmetric stacking of (*M*)-[5]helicene linkers across the repetitive layers (top: complete unit, bottom: single layer); (e) top and side view of the corresponding statistical model $(AA_i:AB)^{stat}$; (f) example of single hexagonal pore extracted from the structural model; the homochiral (*P*)-**[5]Heli-TFP** COF can be also described with statistical structural model $(AA_i:AB)^{stat}$ (see also Figure S62).

distribution of AA-inclined:AB-staggered [$(AA_i:AB)^{stat}$] stacking modes (Figure 4d).[137] These multilayer statistical representations with interlayer shifts have been proposed for isoenergetic ensembles in 2D COFs.[138-141] In this case, the multilayer model $(AA_{inc}:AB)^{stat}$ shows the best agreement with the experimental PXRD diffractograms for both homochiral (*P*)- and (*M*)-**[5]Heli-TFP** COFs (Figures S59-63). In contrast, other hexagonal single-stacking modes exhibited a prominent main reflex in $2\theta = 2.4°$, which did not match with the experimental PXRD patterns (table S9 and S10). In our proposed statistical model $(AA_i:AB)^{stat}$, the ideal columnar packing of enantiopure [5]helicenes units with their helical axes parallel,[127, 128] may generate local dipole moments perpendicular to the *c*-axis, disturbing the ideal AA_i stacking mode. Consequently, adjacent homochiral layers avoid their repulsion by adopting a structurally alternating AB-staggered stacking mode with enantiopure [5]helicene cores irregularly shifted on top of each other (Figure 4d). Our suggested multilayer representation $(AA_i:AB)^{stat}$ decreases the proximity of enantiopure [5]helicene cores and minimizes the steric hindrance between the homochiral layers, leading to a reduced packing density (Figure 4e-f). Homochiral (*P*)- and (*M*)-**[5]Heli-TFP** COFs form less compact asymmetric lattices and exhibit a lower degree of crystallinity than their racemic counterparts, in agreement with Liebisch–Wallach's rule.[79]

The distinct hexagonal structural models for the homochiral and racemic **[5]Heli-TFP** COFs should also lead to differences in the physical properties of the solids. For instance, entirely different types of inherent porosity are expected from crystalline lattices with predominantly symmetric hexagonal AA stacking mode than more distorted lattices with AB stacking mode.[142-144] Interestingly, the N_2 sorption measurements from the homochiral (*P*)- and (*M*)-**[5]Heli-TFP** COFs only exhibited a single step below $p/p_0 = 0.1$, which can be associated with microporous materials according to a type I isotherm (Figure 3b).[129] Specifically, (*P*)-**[5]Heli-TFP** COF has a porosity value of SA_{BET} = 422 $m^2 g^{-1}$ (Figure S25),[130] and a pore size distribution estimated around 17.4 Å (Figure S29). Nearly identically, (*M*)-**[5]Heli-TFP** COF shows a porosity value of SA_{BET} = 440 $m^2 g^{-1}$ (Figure S26),[130] with a pore size distribution estimated around 16.1 Å (Figure S30). In contrast,

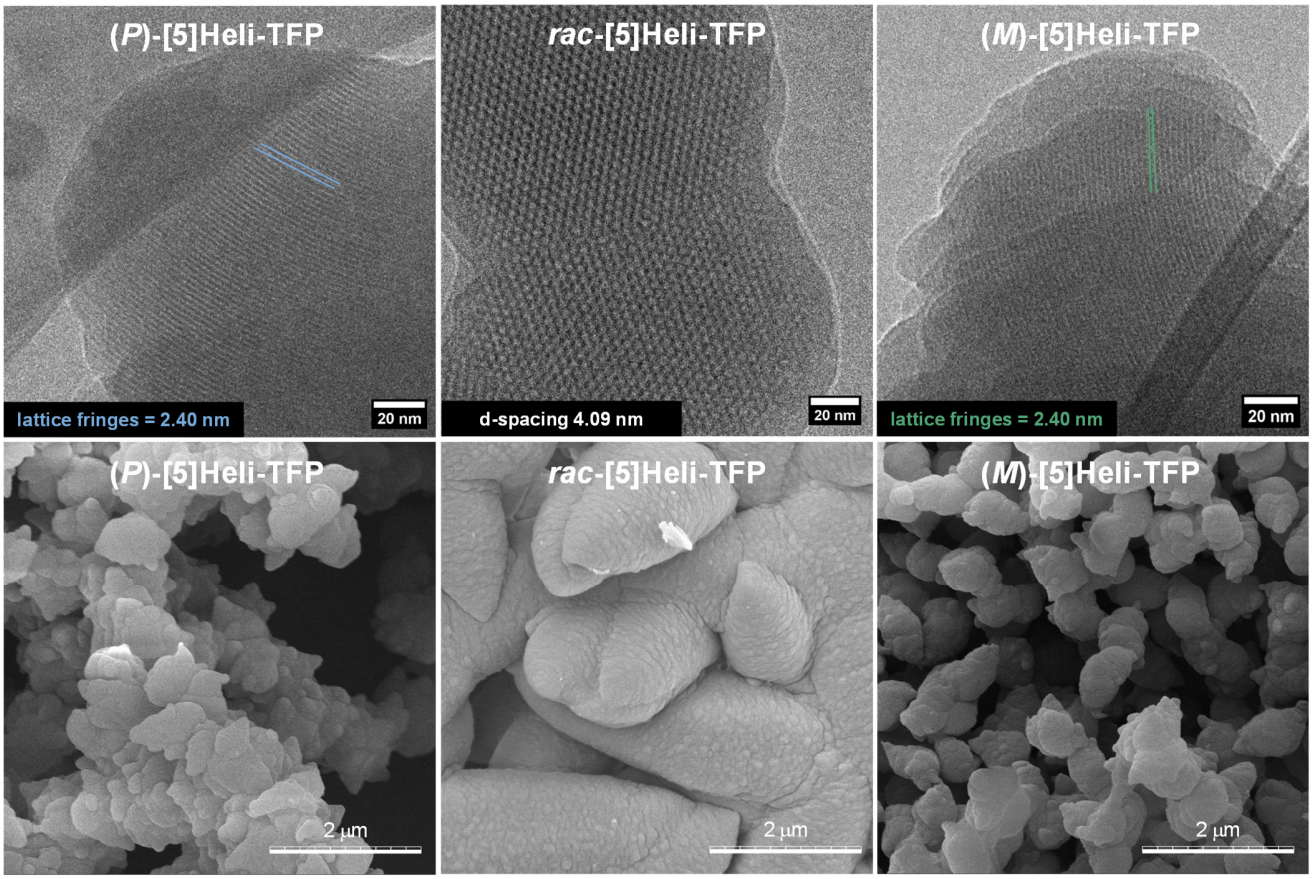

Figure 5. Comparison of the morphology from the homochiral and racemic **[5]Heli-TFP** COFs powders; (top) Low-dose cryo-HR-TEM images at 77 K of (*P*)-**[5]Heli-TFP** COF, *rac*-**[5]Heli-TFP** COF, and (*M*)-**[5]Heli-TFP** COF; (bottom) corresponding FE-SEM micrographs of **[5]Heli-TFP** COFs samples at 298 K, showing different features and size particles between each other.

rac-**[5]Heli-TFP** COF is a mesoporous solid which exhibits significantly higher N_2 uptake, and larger pore size compared to the homochiral analogues (Figure 3b). The observed differences in porosity types between racemic and homochiral **[5]Heli-TFP** COFs are in agreement with their corresponding proposed stacking models — where highly symmetric hexagonal lattices with an AA-inclined stacking mode generally have greater porosity values compared to less-ordered lattices with an AB stacking mode.[142-144]

Subsequently, the comparison of the morphology and features of the homochiral and racemic **[5]Heli-TFP** COFs was performed. In this case, low-dose cryo-HR-TEM of exfoliated homochiral samples revealed regular lattice fringes of around 2.4 nm spacing (most likely viewed across the pore channels) (Figure 5, top). Using Bragg's equation,[145] the visualized lattice fringes can be associated with their relative intense reflex in PXRD at $2\theta = 4.2°$, confirming the crystalline nature of homochiral 2D **[5]Heli-TFP** COFs. Next, the physical features of homochiral and racemic **[5]Heli-TFP** COFs were compared by FE-SEM micrographs (Figure 5, bottom). There, the homochiral solids showed homogenous particles similar to each other (average length 0.9 μm and 0.7 μm, respectively), with a pointed star-shape, and spike-like surface. In contrast, *rac*-**[5]Heli-TFP** COF displays mesh-type conglomerates with variable elongations and rounded features with a soft-like surface (average rod diameter = 2.7 μm). In contrast to these observations, the elemental analysis of both homochiral and racemic **[5]Heli-TFP** COFs reveals an almost identical chemical composition (Table S7). Hence, our results suggest that the structural and physical properties of homochiral and racemic **[5]Heli-TFP** COFs are mainly directed by the absolute configuration of their respective [5]helicene-based linkers.

To confirm the structural differences between homochiral and racemic **[5]Heli-TFP** COFs, their chiroptical properties were analyzed. As an initial comparison, the ECD spectra of the enantiomerically pure building blocks (*P*)-(–)-**3** and (*M*)-(+)-**3** exhibited mirror-imaged Cotton effects in the UV-Vis range (250–450 nm) (Figure 6). In contrast, the averaged ECD spectra for the homochiral (*P*)- and (*M*)-**[5]Heli-TFP** COFs showed an intense first Cotton effect in the visible region from 470 nm up to ca. 800 nm (Figure 6). Specifically, the (*P*)-**[5]Heli-TFP** COF displayed a first positive Cotton effect at 504 nm and a second negative Cotton effect at 406 nm. Satisfyingly, the homochiral analogue (*M*)-**[5]Heli-TFP** COF showed the opposite signed ECD pattern with a first negative Cotton effect at 502 nm, and a second intense positive Cotton effect at 411 nm. In this case, the observed ECD bands below 470 nm can be associated with the inherent helical chirality from the corresponding enantiopure [5]helicene *pseudo*-C_2 linkers, supported by TD-DFT simulations of a small (*P*)-**[5]Heli-TFP** COF fragment (Figure S74). In contrast, the broad ECD signals exceeding 800 nm, possibly arise from the extended helical arrangement in the homochiral 2D lattices, as a result of delocalized exciton formation over the asymmetric conjugated lattices.[146, 147] As

expected, *rac*-**[5]Heli-TFP** COF remains chiroptically silent confirming its racemic composition.

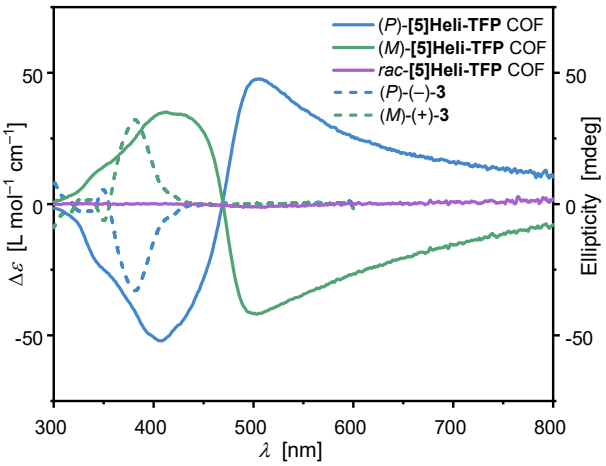

Figure 6. Chiroptical properties of enantiopure building blocks, homochiral and racemic **[5]Heli-TFP** COFs. ECD spectra of the enantiopure building blocks (*P*)-(–)-**3** and (*M*)-(+)-**3** in CH_2Cl_2 (c = 1.1×10^{-6} M at 298 K, dashed traces – $\Delta\varepsilon$ ordinate); average ECD spectra of *rac*-**[5]Heli-TFP** COF, (*P*)- and (*M*)-**[5]Heli-TFP** COFs ($c \approx 0.08$ g L^{-1}) as DMSO dispersions, averaged over different rotation angles at 298 K (solid traces – ellipticity ordinate; see also Figures S70–72).

Conclusion

In summary, we synthesized both homochiral and racemic 2D COFs from enantiopure and racemic [5]helicene derivatives introducing helical chirality into the backbone of all-organic homochiral 2D COFs. Our findings confirm that the absolute stereochemistry directs the structural characteristics and properties of crystallized 2D carbon-based lattices between homochiral and racemic 2D COFs. Specifically, racemic [5]helicene linkers promote the formation of highly crystalline and porous 2D frameworks with a predominant AA-inclined stacking mode, attributed to the locally dense packing of racemic motifs, such as *rac*-**[5]HeliCOF-TFB** and *rac*-**[5]HeliCOF-TFP**. In contrast, enantiopure [5]helicene building blocks yield an asymmetric hexagonal structure, mainly represented by a multilayer model $(AA_i{:}AB)^{stat}$ with a lower degree of crystallinity and reduced accessible porosity compared to their racemic counterpart. Our observations mark the expansion of the Liebisch–Wallach rule to all-organic 2D frameworks, demonstrating that the absolute stereochemical composition of carbon-based building blocks can significantly influence the stacking interaction of crystalline and porous 2D lattices.

The homochiral (*P*)- and (*M*)-**[5]Heli-TFP** COFs exhibited extended Cotton effects, reaching beyond 800 nm, attributed to the propagation of helical chirality from the [5]helicenylene into the backbone of the 2D frameworks. Future work will explore the chiral emission properties of such homochiral **[5]HeliCOFs** using highly-emissive building blocks. We expect a broad fundamental applicability of our findings to novel chiroptical characteristics and potential applications of crystalline and porous 2D homochiral organic solids and thin films.

ASSOCIATED CONTENT

Supporting Information.
The Supporting Information is available free of charge. Detailed information on experimental methods, materials used, synthetic characterization, calculation data, and atomic coordinates of the frameworks.

AUTHOR INFORMATION

Corresponding Author

* Oliver Dumele
Department of Organic Chemistry, Albert-Ludwigs-Universität Freiburg, Albertstrasse 21, 79104 Freiburg, Germany

Freiburg Materials Research Center (FMF), Albert-Ludwigs-Universität Freiburg, Stefan-Meier-Strasse 21, 79104 Freiburg, Germany

Freiburg Center for Interactive Materials and Bioinspired Technologies (FIT), Albert-Ludwigs-Universität Freiburg, Georges-Köhler-Allee 105, 79110 Freiburg, Germany

Department of Chemistry, Humboldt University of Berlin, Brook-Taylor-Strasse 2, 12489 Berlin, Germany.

Email: oliver.dumele@oc.uni-freiburg.de

Authors

José del Refugio Monroy – Department of Chemistry & Center for the Science of Materials Berlin, Humboldt University of Berlin, Brook-Taylor-Strasse 2, 12489 Berlin, Germany. Department of Organic Chemistry, Albert-Ludwigs-Universität Freiburg, Albertstrasse 21, 79104 Freiburg, Germany

Joël Schlecht – Department of Organic Chemistry, Albert-Ludwigs-Universität Freiburg, Albertstrasse 21, 79104 Freiburg, Germany

Clara Douglas – Department of Organic Chemistry, Albert-Ludwigs-Universität Freiburg, Albertstrasse 21, 79104 Freiburg, Germany.

Robbie Stirling – Department of Chemistry & Center for the Science of Materials Berlin, Brook-Taylor-Strasse 2, 12489 Berlin, Germany

Glen J. Smales – Bundesanstalt für Materialforschung und -prüfung, Unter den Eichen 87, 12205 Berlin, Germany.

Zdravko Kochovski – Department for Electrochemical Energy Storage, Helmholtz-Zentrum Berlin für Materialien und Energie, Hahn-Meitner-Platz 1, 14109 Berlin, Germany.

Notes. The authors declare no competing financial interest.

ACKNOWLEDGMENTS

We thank Dr. Björn Kobin for assistance with the synthetic irradiation setup, Sebastian Pallasch for TGA measurements, Prof. Philipp Adelhelm for proving access to SEM, Sven Herter for measuring HR-MS, and Domantas Kuryla for initial experiments. Dr. Burkhard Butschke and Dr. Nils Trapp (ETH Zürich) are acknowledged for insightful crystallographic discussions regarding the absolute structure determination. We are grateful to Stefan Hecht for his support during the recent years. J.R.M. was supported by a doctoral fellowship of the International Max Planck Research

School (IMPRS) on Multiscale Biosystems and a CONAHCYT fellowship. This research was supported by the German Federal Ministry of Education and Research (BMBF BattFutur, 03XP0457). This manuscript is dedicated to the memory of Prof. Dr. Jack D. Dunitz.

References

(1) Yashima, E.; Maeda, Katsushiro.; Iida, Hiroki.; Furuscho, Yoshio.; Nagai, K. Helical Polymers: synthesis, structures, and functions. *J. Am. Chem. Soc.* **2009**, *109*, 6102–6211. DOI: 10.1021/cr900162q.
(2) Rickhaus, M.; Mayor, M.; Juríček, M. Strain-Induced Helical Chirality in Polyaromatic Systems. *Chem. Soc. Rev.* **2016**, *45*, 1542–1556. DOI: 10.1039/C5CS00620A.
(3) Morrow, S. M.; Bissette, A. J.; Fletcher, S. P. Transmission of chirality through space and across length scales. *Nat. Nanotechnol.* **2017**, *12*, 410–419. DOI: 10.1038/nnano.2017.62.
(4) Fernández-García, J. M.; Evans, P. J.; Filippone, S.; Herranz, M. Á.; Martín, N. Chiral Molecular Carbon Nanostructures. *Acc. Chem. Res.* **2019**, *52*, 1565–1574. DOI: 10.1021/acs.accounts.9b00144.
(5) Crassous, J.; Fuchter, M. J.; Freedman, D. E.; Kotov, N. A.; Moon, J.; Beard, M. C.; Feldmann, S. Materials for Chiral Light Control. *Nat. Rev. Mater.* **2023**, *8*, 365–371. DOI: 10.1038/s41578-023-00543-3.
(6) Zhu, H.; Yakobson, B. I. Creating Chirality in the Nearly Two Dimensions. *Nat. Mater.* **2024**, *23*, 316–322.
DOI: 10.1038/s41563-024-01814-2.
(7) Ettl, R.; Chao, I.; Diederich, F.; Whetten, R. L. Isolation of C76, a Chiral (D2) Allotrope of Carbon. *Nature* **1991**, *353*, 149–153. DOI: 10.1038/353149a0.
(8) Schaller, G. R.; Topić, F.; Rissanen, K.; Okamoto, Y.; Shen, J.; Herges, R. Design and Synthesis of the First Triply Twisted Möbius Annulene. *Nat. Chem.* **2014**, *6*, 608–613.
DOI: 10.1038/nchem.1955.
(9) Krzeszewski, M.; Ito, H.; Itami, K. Infinitene: A Helically Twisted Figure-Eight [12]Circulene Topoisomer. *J. Am. Chem. Soc.* **2022**, *144*, 862–871. DOI: 10.1021/jacs.1c10807.
(10) Niu, W.; Fu, Y.; Qiu, Z. L.; Schürmann, C. J.; Obermann, S.; Liu, F.; Popov, A. A.; Komber, H.; Ma, J.; Feng, X. π-Extended Helical Multilayer Nanographenes with Layer-Dependent Chiroptical Properties. *J. Am. Chem. Soc.* **2023**, *145*, 26824–26832.
DOI: 10.1021/jacs.3c09350.
(11) Liu, K.; Zheng, W.; Osella, S.; Qiu, Z. L.; Böckmann, S.; Niu, W.; Meingast, L.; Komber, H.; Obermann, S.; Gillen, R.; Bonn, M.; Hansen, M. R.; Maultzsch, J.; Ma, W. J.; Feng, X. Cove-Edged Chiral Graphene Nanoribbons with Chirality-Dependent Bandgap and Carrier Mobility. *J. Am. Chem. Soc.* **2024**, *146*, 1026–1034.
DOI: 10.1021/jacs.3c11975.
(12) Natta, G.; Pino, P.; Corradini, P.; Danusso, F.; Mantica, E.; Mazzanti, G.; Moraglio, G. Crystalline High Polymers of α-Olefins. *J. Am. Chem. Soc.* **1955**, *77*, 1708–1710. DOI: 10.1021/ja01611a109.
(13) Green, M. M.; Peterson, N. C.; Sato, T.; Teramoto, A.; Cook, R.; Lifson, S. A Helical Polymer with a Cooperative Response to Chiral Information. *Science* **1995**, *268*, 1860–1866.
DOI: 10.1126/science.268.5219.1860.
(14) Bodenhöfer, K.; Hierlemann, A.; Seemann, J.; Gauglitz, G.; Koppenhoefer, B.; Gpel, W. Chiral discrimination using piezoelectric and optical gas sensors. *Nature* **1997**, *387*, 577–580. DOI: 10.1038/42426.
(15) Sakurai, S. I.; Okoshi, K.; Kumaki, J.; Yashima, E. Two-Dimensional Surface Chirality Control by Solvent-Induced Helicity Inversion of a Helical Polyacetylene on Graphite. *J. Am. Chem. Soc.* **2006**, *128*, 5650–5651. DOI: 10.1021/ja061238b.
(16) Wehner, M.; Röhr, M. I. S.; Stepanenko, V.; Würthner, F. Control of self-assembly pathways toward conglomerate and racemic supramolecular polymers. *Nat. Commun*. **2020**, *11*, 5460.
DOI: 10.1038/s41467-020-19189-8.
(17) Song, I.; Ahn, J.; Ahn, H.; Lee, S. H.; Mei, J.; Kotov, N. A.; Oh, J. H. Helical polymers for dissymmetric circularly polarized light imaging. *Nature* **2023**, *617*, 92–99. DOI: 10.1038/s41586-023-05877-0.
(18) Tan, K. K.; Guo, W. C.; Zhao, W. L.; Li, M.; Chen, C. F. Self-Assembled Chiral Polymers Exhibiting Amplified Circularly Polarized Electroluminescence. *Angew. Chem. Int. Ed.* **2024**, e202412283. DOI: 10.1002/anie.202412283.
(19) Hirschberg, J. H. K. K.; Brunsveld, L.; Ramzi, A.; Vekemans, J. A. J. M.; Sijbesma, R. P.; Meijer, E. W. Helical self-assembled polymers from cooperative stacking of hydrogen-bonded pairs. *Nature* **2000**, *407*, 167–170. DOI: 10.1038/35025027.
(20) Li, X.; Hu, W.; Wang, Y.; Quan, Y.; Cheng, Y. Strong CPL of achiral AIE-active dyes induced by supramolecular self-assembly in chiral nematic liquid crystals. *Chem. Commun.* **2019**, *55*, 5179–5182.
DOI: 10.1039/C9CC01678C.
(21) Ślęczkowski, M. L.; Mabesoone, M. F. J.; Ślęczkowski, P.; Palmans, A. R. A.; Meijer, E. W. Competition between chiral solvents and chiral monomers in the helical bias of supramolecular polymers. *Nat. Chem.* **2021**, *13*, 200–207.
DOI: 10.1038/s41557-020-00583-0.
(22) Ueda, M.; Aoki, T.; Akiyama, T.; Nakamuro, T.; Yamashita, K.; Yanagisawa, H.; Nureki, O.; Kikkawa, M.; Nakamura, E.; Aida, T.; Itoh, Y. Alternating Heterochiral Supramolecular Copolymerization. *J. Am. Chem. Soc.* **2021**, *143*, 5121–5126.
DOI: 10.1021/jacs.1c00823.
(23) Xu, F.; Crespi, S.; Pacella, G.; Fu, Y.; Stuart, M. C. A.; Zhang, Q.; Portale, G.; Feringa, B. L. Dynamic Control of a Multistate Chiral Supramolecular Polymer in Water. *J. Am. Chem. Soc.* **2022**, *144*, 6019–6027. DOI: 10.1021/jacs.2c01063.
(24) Sun, R.; Park, K. S.; Comstock, A. H.; McConnell, A.; Chen, Y. C.; Zhang, P.; Beratan, D.; You, W.; Hoffmann, A.; Yu, Z. G.; Diao, Y.; Sun, D. Inverse Chirality-Induced Spin Selectivity Effect in Chiral Assemblies of π-conjugated Polymers. *Nat. Mater.* **2024**, s41563. DOI: 10.1038/s41563-024-01838-8.
(25) Green, M. M.; Park, J. W.; Sato, T.; Teramoto, A.; Lifson, S.; Selinger, R. L. B.; Selinger, J. V. The Macromolecular Route to Chiral Amplification. *Angew. Chem. Int. Ed.* **1999**, *38*, 3138–3154.
DOI: 10.1002/(SICI)1521-3773(19991102)38:21<3138::AID-ANIE3138>3.0.CO;2-C.
(26) Cobos, K.; Rodríguez, R.; Quiñoá, E.; Riguera, R.; Freire, F. From Sergeants and Soldiers to Chiral Conflict Effects in Helical Polymers by Acting on the Conformational Composition of the Comonomers. *Angew. Chem. Int. Ed.* **2020**, *59*, 23724–23730.
DOI: 10.1002/anie.202009215.
(27) Greenfield, J. L.; Wade, J.; Brandt, J. R.; Shi, X.; Penfold, T. J.; Fuchter, M. J. Pathways to increase the dissymmetry in the interaction of chiral light and chiral molecules. *Chem. Sci.* **2021**, *12*, 8589–8602.
DOI: 10.1039/D1SC02335G.
(28) Chen, T. L.; Salij, A.; Parrish, K. A.; Rasch, J. K.; Zinna, F.; Brown, P. J.; Pescitelli, G.; Urraci, F.; Aronica, L. A.; Dhavamani, A.; Arnold, M. S.; Wasielewski, M. R.; di Bari, L.; Tempelaar, R. Goldsmith, R. H. A 2D Chiral Microcavity Based on Apparent Circular Dichroism. *Nat. Commun.* **2024**, *15*, 3072–3083.
DOI: 10.1038/s41467-024-47411-4.
(29) Kepert, C. J.; Prior, T. J.; Rosseinsky, M. J. A Versatile Family of Interconvertible Microporous Chiral Molecular Frameworks: The First Example of Ligand Control of Network Chirality. *J. Am. Chem. Soc.* **2000**, *122*, 5158–5168. DOI: 10.1021/ja993814s.
(30) Morris, R. E.; Bu, X. Induction of chiral porous solids containing only achiral building blocks. *Nature Chem.* **2010**, *2*, 353–361. DOI: 10.1038/nchem.628.
(31) Dong, J.; Liu, Y.; Cui, Y. Emerging chiral two-dimensional materials. *Nat. Chem.* **2024**, *16*, 1398–1407.
DOI: 10.1038/s41557-024-01595-w.
(32) Diercks, C. S.; Yaghi, O. M. The Atom, the Molecule, and the Covalent Organic Framework. *Science* **2017**, *355*, eaal1585.
DOI: 10.1126/science.aal1585.
(33) Tan, K. T.; Ghosh, S.; Wang, Z.; Wen, F.; Rodríguez-San-Miguel, D.; Feng, J.; Huang, N.; Wang, W.; Zamora, F.; Feng, X.; Thomas, A.; Jiang, D. Covalent Organic Frameworks. *Nat. Rev. Methods Primers.* **2023**, *3*. DOI: 10.1038/s43586-022-00181-z.

(34) Xu, H. S.; Ding, S. Y.; An, W. K.; Wu, H.; Wang, W. Constructing Crystalline Covalent Organic Frameworks from Chiral Building Blocks. *J. Am. Chem. Soc.* **2016**, *138*, 11489–11492. DOI: 10.1021/jacs.6b07516.
(35) Wang, X.; Han, X.; Zhang, J.; Wu, X.; Liu, Y.; Cui, Y. Homochiral 2D Porous Covalent Organic Frameworks for Heterogeneous Asymmetric Catalysis. *J. Am. Chem. Soc.* **2016**, *138*, 12332–12335. DOI: 10.1021/jacs.6b07714.
(36) Wang, R. Q.; Wei, X. B.; Feng, Y. Q. β-Cyclodextrin Covalent Organic Framework for Selective Molecular Adsorption. *Chem. Eur. J.* **2018**, *24*, 10979–10983. DOI: 10.1002/chem.201802564.
(37) Xu, H.; Chen, X.; Gao, J.; Lin, J.; Addicoat, M.; Irle, S.; Jiang, D. Catalytic Covalent Organic Frameworks Via Pore Surface Engineering. *Chem. Commun.* **2014**, *50*, 1292–1294. DOI: 10.1039/C3CC48813F.
(38) Qian, H. L.; Yang, C. X.; Yan, X. P. Bottom-up synthesis of chiral covalent organic frameworks and their bound capillaries for chiral separation. *Nat. Commun.* **2016**, *7*, 12104. DOI: 10.1038/ncomms12104.
(39) Zhang, J.; Han, X.; Wu, X.; Liu, Y.; Cui, Y. Multivariate Chiral Covalent Organic Frameworks with Controlled Crystallinity and Stability for Asymmetric Catalysis. *J. Am. Chem. Soc.* **2017**, *139*, 8277–8285. DOI: 10.1021/jacs.7b03352.
(40) Wang, L. K.; Zhou, J. J.; Lan, Y.-B.; Ding, S. Y.; Yu, W.; Wang, W. Divergent Synthesis of Chiral Covalent Organic Frameworks. *Angew. Chem. Int. Ed.* **2019**, *58*, 9443–9447. DOI: 10.1002/anie.201903534.
(41) Song, Q.; Yang, J.; Zheng, K.; Zhang, T.; Yuan, C.; Yuan, L. M.; Hou, X. Chiral Memory in Dynamic Transformation from Porous Organic Cages to Covalent Organic Frameworks for Enantiorecognition Analysis. *J. Am. Chem. Soc.* **2024**, 7594–7604. DOI: 10.1021/jacs.3c13692.
(42) Tang, X.; Zha, J.; Wu, X.; Tong, J.; Gu, Q.; Zhang, K.; Zhang, Y.; Zheng, S.; Fan, J.; Zhang, W.; Zhang, Q:, Tan, C.; Cai, S. Construction of Chiral Covalent Organic Frameworks Through a Linker Decomposition Chiral Induction Strategy for Circularly Polarized Light Detection. *Angew. Chem. Int. Ed.* **2024**, e202413675. DOI: 10.1002/anie.202413675.
(43) Han, X.; Xia, Q.; Huang, J.; Liu, Y.; Tan, C.; Cui, Y. Chiral Covalent Organic Frameworks with High Chemical Stability for Heterogeneous Asymmetric Catalysis. *J. Am. Chem. Soc.* **2017**, *139*, 8693–8697. DOI: 10.1021/jacs.7b04008.
(44) Wang, J. C.; Kan, X.; Shang, J. Y.; Qiao, H.; Dong, Y. B. Catalytic Asymmetric Synthesis of Chiral Covalent Organic Frameworks from Prochiral Monomers for Heterogeneous Asymmetric Catalysis. *J. Am. Chem. Soc*. **2020**, *142*, 16915–16920. DOI: 10.1021/jacs.0c07461.
(45) Weng, W.; Guo, J. The Effect of Enantioselective Chiral Covalent Organic Frameworks and Cysteine Sacrificial Donors on Photocatalytic Hydrogen Evolution. *Nat. Commun.* **2022**, *13*, 5768–5779. DOI: 10.1038/s41467-022-33501-8.
(46) Ma, H. C.; Sun, Y. N.; Chen, G. J.; Dong, Y. B. A BINOL-phosphoric acid and metalloporphyrin derived chiral covalent organic framework for enantioselective α-benzylation of aldehydes. *Chem. Sci.* **2022**, *13*, 1906–1911. DOI: 10.1039/D1SC06045G.
(47) Zhang, Y. J.; Li, L. H.; Feng, J.; Deng, X.; Sun, T.; Huang, J. F.; Fan, Y. Q.; Lan, Y. B.; Wang, Z. P.; Li, X. M.; Liang, L.; Ding, S. Y.; Ma, Y. H.; Peng, Y.; Wang, W. Observation of Chiral Channels in Helical Covalent Organic Frameworks. *J. Am. Chem. Soc.* **2024**. DOI: 10.1021/jacs.4c01969.
(48) Zhang, S.; Zheng, Y.; An, H.; Aguila, B.; Yang, C.-X.; Dong, Y.; Xie, W.; Cheng, P.; Zhang, Z.; Chen, Y.; Ma, S. Covalent Organic Frameworks with Chirality Enriched by Biomolecules for Efficient Chiral Separation. *Angew. Chem. Int. Ed.* **2018**, *57*, 16754–16759. DOI: 10.1002/anie.201810571.
(49) Li, M.; Qiao, S.; Zheng, Y.; Andaloussi, Y. H.; Li, X.; Zhang, Z.; Li, A.; Cheng, P.; Ma, S.; Chen, Y. Fabricating Covalent Organic Framework Capsules with Commodious Microenvironment for Enzymes. *J. Am. Chem. Soc.* **2020**, *142*, 6675–6681. DOI: 10.1021/jacs.0c00285.
(50) Han, X.; Zhang, J.; Huang, J.; Wu, X.; Yuan, D.; Liu, Y.; Cui, Y. Chiral Induction in Covalent Organic Frameworks. *Nat. Commun.* **2018**, *9*, 1294–1304. DOI: 10.1038/s41467-018-03689-9.
(51) Li, F.; Kan, J. L.; Yao, B. J.; Dong, Y. B. Synthesis of Chiral Covalent Organic Frameworks via Asymmetric Organocatalysis for Heterogeneous Asymmetric Catalysis. *Angew. Chem. Int. Ed.* **2022**, *61*, e202115044. DOI: 10.1002/anie.202115044.
(52) Zha, X.; Xu, G.; Khan, N. A.; Yan, Z.; Zuo, M.; Xiong, Y.; Liu, Y.; You, H.; Wu, Y.; Liu, K.; Li, M.; Wang, D. Sculpting Mesoscopic Helical Chirality into Covalent Organic Framework Nanotubes from Entirely Achiral Building Blocks. *Angew. Chem. Int. Ed.* **2024**, *63*, e202316385. DOI: 10.1002/anie.202316385.
(53) Yuan, C.; Jia, W.; Yu, Z.; Li, Y.; Zi, M.; Yuan, L. M.; Cui, Y. Are Highly Stable Covalent Organic Frameworks the Key to Universal Chiral Stationary Phases for Liquid and Gas Chromatographic Separations? *J. Am. Chem. Soc.* **2022**, *144*, 891–900. DOI: 10.1021/jacs.1c11051.
(54) Xu, J.; Feng, G.; Ao, D.; Li, X.; Li, M.; Lei, S.; Wang, Y. Functional Covalent Organic Frameworks' Microspheres Synthesized by Self-Limited Dynamic Linker Exchange for Stationary Phases. *Adv. Mater.* **2024**, *36*, 2406256. DOI: 10.1002/adma.202406256.
(55) Xu, H.; Gao, J.; Jiang, D. Stable, crystalline, porous, covalent organic frameworks as a platform for chiral organocatalysts. *Nat. Chem.* **2015**, *7*, 905–912. DOI: 10.1038/nchem.2352.
(56) He, T.; On, I. K. W.; Bi, S.; Huang, Z.; Guo, J.; Wang, Z.; Zhao, Y. Crystalline Olefin-Linked Chiral Covalent Organic Frameworks as a Platform for Asymmetric Catalysis. *Angew. Chem. Int. Ed.* **2024**, *63*, e202405769. DOI: 10.1002/anie.202405769.
(57) Li, J.; Zhang, K.; Tang, X.; Yang, X.; Chen, H.; Zheng, S.; Fan, J.; Xie, M.; Zhang, W.; Li, X.; Cai, S. Primary Amine-Functionalized Chiral Covalent Organic Framework Enables High-Efficiency Asymmetric Catalysis in Water. *ACS Appl. Mater. Interfaces*. **2024**, *16*, 59379–59387. DOI: 10.1021/acsami.4c14161.
(58) Chen, H.; Gu, Z. G.; Zhang, J. Chiral-Induced Ultrathin Covalent Organic Frameworks Nanosheets with Tunable Circularly Polarized Luminescence. *J. Am. Chem. Soc.* **2022**, *144*, 7245–7252. DOI: 10.1021/jacs.2c00285.
(59) Tang, X.; Liao, X.; Cai, X.; Wu, J.; Wu, X.; Zhang, Q.; Yan, Y.; Zheng, S.; Jiang, H.; Fan, J.; Cai, S.; Zhang, W.; Liu, Y. Self-Assembly of Helical Nanofibrous Chiral Covalent Organic Frameworks. *Angew. Chem. Int. Ed.* **2023**, *62*, e202216310. DOI: 10.1002/anie.202216310.
(60) Tang, X.; Zhang, K.; Xue, R.; Zheng, Y.; Chen, S.; Zheng, S.; Fan, J.; Zhang, Y.; Ye, W.; Zhang, W.; Cai, S.; Liu, Y. Self-Standing Chiral Covalent Organic Framework Thin Films with Full-Color Tunable Guest-Induced Circularly Polarized Luminescence. *Angew. Chem. Int. Ed.* **2024**, e202413171. DOI: 10.1002/anie.202413171.
(61) Yan, C.; Li, Q.; Wang, K.; Yang, W.; Han, J.; Li, Y.; Dong, Y.; Chu, D.; Cheng, L.; Cao, L. "Gear-driven"-type chirality transfer of tetraphenylethene-based supramolecular organic frameworks for peptides in water. *Chem. Sci.* **2024**, *15*, 3758–3766, 10.1039/D3SC06349F. DOI: 10.1039/D3SC06349F.
(62) Weng, W.; Guo, J. Chiral Covalent Organic Framework Films with Enhanced Photoelectrical Performances. *J. Am. Chem. Soc.* **2024**, *146*, 13201–13209. DOI: 10.1021/jacs.4c01097.
(63) Han, X.; Jiang, C.; Hou, B.; Liu, Y.; Cui, Y. Covalent Organic Frameworks with Tunable Chirality for Chiral-Induced Spin Selectivity. *J. Am. Chem. Soc.* **2024**, 6733–6743. DOI: 10.1021/jacs.3c13032.
(64) Martínez-Abadía, M.; Stoppiello, C. T.; Strutynski, K.; Lerma-Berlanga, B.; Martí-Gastaldo, C.; Saeki, A.; Melle-Franco, M.; Khlobystov, A. N.; Mateo-Alonso, A. A Wavy Two-Dimensional Covalent Organic Framework from Core-Twisted Polycyclic Aromatic Hydrocarbons. *J. Am. Chem. Soc.* **2019**, *141*, 14403–14410. DOI: 10.1021/jacs.9b07383.
(65) Yu, J. T.; Chen, Z.; Sun, J.; Huang, Z. T.; Zheng, Q. Y. Cyclotricatechylene Based Porous Crystalline Material: Synthesis and Applications in Gas Storage. *J. Mater.* **2012**, *22*, 5369–5373. DOI: 10.1039/C2JM15159F.
(66) Thompson, C. M.; Occhialini, G.; McCandless, G. T.; Alahakoon, S. B.; Cameron, V.; Nielsen, S. O.; Smaldone, R. A. Computational and Experimental Studies on the Effects of Monomer Planarity on Covalent

Organic Framework Formation. *J. Am. Chem. Soc.* **2017**, *139*, 10506–10513. DOI: 10.1021/jacs.7b05555.
(67) Shan, Z.; Wu, M.; Gu, Z.; Nishiyama, Y.; Zhang, G. A non-planar 2D covalent organic framework derived from a Z-shaped building unit. *Chem. Commun.* **2021**, *57*, 9236–9239.
DOI: 10.1039/D1CC04103G.
(68) Jin, E.; Fu, S.; Hanayama, H.; Addicoat, M. A.; Wei, W.; Chen, Q.; Graf, R.; Landfester, K.; Bonn, M.; Zhang, K. A. I.; Wang, H. I.; Müllen, K.; Narita, A. A Nanographene-Based Two-Dimensional Covalent Organic Framework as a Stable and Efficient Photocatalyst. *Angew. Chem. Int. Ed.* **2022**, *61*, e202114059.
DOI: 10.1002/anie.202114059.
(69) Xing, G.; Zheng, W.; Gao, L.; Zhang, T.; Wu, X.; Fu, S.; Song, X.; Zhao, Z.; Osella, S.; Martínez-Abadía, M.; Wang, H. I.; Cai, J.; Mateo-Alonso, A.; Chen, L. Nonplanar Rhombus and Kagome 2D Covalent Organic Frameworks from Distorted Aromatics for Electrical Conduction. *J. Am. Chem. Soc.* **2022**, *144*, 5042–5050.
DOI: 10.1021/jacs.1c13534.
(70) Yan, Q.; Tao, S.; Liu, R.; Zhi, Y.; Jiang, D. Crystalline, Porous Helicene Covalent Organic Frameworks. *Angew. Chem. Int. Ed.* **2024**, *63*, e202316092. DOI: 10.1002/anie.202316092.
(71) Yin, C.; Ye, X.; Tao, S.; Zhao, D.; Zhi, Y.; Jiang, D. Helicene Covalent Organic Frameworks for Robust Light Harvesting and Efficient Energy Transfers. *Angew. Chem. Int. Ed.* **2024**, *63*, e202411558. DOI: 10.1002/anie.202411558.
(72) Wu, X.; Han, X.; Xu, Q.; Liu, Y.; Yuan, C.; Yang, S.; Liu, Y.; Jiang, J.; Cui, Y. Chiral BINOL-Based Covalent Organic Frameworks for Enantioselective Sensing. *J. Am. Chem. Soc.* **2019**, *141*, 7081–7089.
DOI: 10.1021/jacs.9b02153.
(73) Yuan, C.; Fu, S.; Yang, K.; Hou, B.; Liu, Y.; Jiang, J.; Cui, Y. Crystalline C—C and C═C Bond-Linked Chiral Covalent Organic Frameworks. *J. Am. Chem. Soc.* **2021**, *143*, 369–381.
DOI: 10.1021/jacs.0c11050.
(74) Du, C.; Zhu, X.; Yang, C.; Liu, M. Stacked Reticular Frame Boosted Circularly Polarized Luminescence of Chiral Covalent Organic Frameworks. *Angew. Chem. Int. Ed.* **2022**, *61*, e202113979.
DOI: 10.1002/anie.202113979.
(75) Sánchez-Fuente, M.; López-Magano, A.; Moya, A.; Mas-Ballesté, R. Stabilized Chiral Organic Material Containing BINAP Oxide Units as a Heterogeneous Asymmetric Organocatalyst for Allylation of Aldehydes. *ACS Appl. Mater. Interfaces.* **2023**, *15*, 30212–30219. DOI: 10.1021/acsami.3c04430.
(76) Zhang, X.; Chen, X.; Fu, S.; Cao, Z.; Gong, W.; Liu, Y.; Cui, Y. Homochiral π-Rich Covalent Organic Frameworks Enabled Chirality Imprinting in Conjugated Polymers: Confined Polymerization and Chiral Memory from Scratch. *Angew. Chem. Int. Ed.* **2024**, *63*, e202403878. DOI: 10.1002/anie.202403878.
(77) Haase, F.; Lotsch, B. V. Solving the COF trilemma: towards crystalline, stable and functional covalent organic frameworks. *Chem. Soc. Rev.* **2020**, *49*, 8469–8500. DOI: 10.1039/D0CS01027H.
(78) Yang, J.; Kang, F.; Wang, X.; Zhang, Q. Design strategies for improving the crystallinity of covalent organic frameworks and conjugated polymers: a review. *Mater.* **2022**, *9*, 121–146.
DOI: 10.1039/D1MH00809A.
(79) Wallach, O. Zur Kenntniss der Terpene und der ätherischen Oele. *Justus Liebigs Ann. Chem.* **1895**, *286*, 90−118.
DOI: 10.1002/jlac.18952860105.
(80) Ernst, K. H. On the Density of Racemic and Homochiral Crystals: Wallach, Liebisch and Sommerfeld in Göttingen. *CHIMIA* **2018**, *72*, 399–403. DOI: 10.2533/chimia.2018.399.
(81) Brock, C. P.; Schweizer, W. B.; Dunitz, J. D. On the validity of Wallach's rule: on the density and stability of racemic crystals compared with their chiral counterparts. *J. Am. Chem. Soc.* **1991**, *113*, 9811–9820. DOI: 10.1021/ja00026a015.
(82) Gavezzotti, A.; Rizzato, S. Are Racemic Crystals Favored over Homochiral Crystals by Higher Stability or by Kinetics? Insights from Comparative Studies of Crystalline Stereoisomers. *J. Org. Chem.* **2014**, *79*, 4809–4816. DOI: 10.1021/jo500528k.
(83) Seki, S.; Paitandi, R. P.; Choi, W.; Ghosh, S.; Tanaka, T. Electron Transport over 2D Molecular Materials and Assemblies. *Acc. Chem. Res.* **2024**. DOI: 10.1021/acs.accounts.4c00376.
(84) Marciniak, J.; Andrzejewski, M.; Cai, W.; Katrusiak, A. Wallach's Rule Enforced by Pressure in Mandelic Acid. *J. Phys. Chem. C.* **2014**, *118*, 4309–4313. DOI: 10.1021/jp411738p.
(85) Wu, X.; Huang, C. Y.; Chen, D. G.; Liu, D.; Wu, C.; Chou, K. J.; Zhang, B.; Wang, Y.; Liu, Y.; Li, E. Y.; Zhu, W.; Chou, P. T. Exploiting racemism enhanced organic room-temperature phosphorescence to demonstrate Wallach's rule in the lighting chiral chromophores. *Nat. Commun.* **2020**, *11*, 2145.
DOI: 10.1038/s41467-020-15976-5.
(86) Yu, M. N.; Li, Y. X.; Xu, M.; Lin, J. Y.; Gu, J. B.; Sun, N.; Lin, D. Q.; Wang, Y. X.; Xie, L. H.; Huang, W. Molecular conformational transition of chiral conjugated enantiomers dominated by Wallach's rule. *J. Mater. Chem. C.* **2021**, *9*, 6991–6995.
DOI: 10.1039/D1TC00978H.
(87) Peng Qiu, C.; Luo Xi, M.; Qin Yu, J.; Wang, T.; Bai, B.; Wei Xi, L.; Li, K.; Zang Shuang, Q. Influence of Wallach's Rule on Chiral AIE Systems and Its Application in Cryptographic Information Storage. *CCS Chem.* **2022**, *4*, 3686–3692.
DOI: 10.31635/ccschem.022.202201998.
(88) Cucinotta, A.; Kahlfuss, C.; Minoia, A.; Eyley, S.; Zwaenepoel, K.; Velpula, G.; Thielemans, W.; Lazzaroni, R.; Bulach, V.; Hosseini, M. W.; Mali, K. S.; De Feyter, S. Metal Ion and Guest-Mediated Spontaneous Resolution and Solvent-Induced Chiral Symmetry Breaking in Guanine-Based Metallosupramolecular Networks. *J. Am. Chem. Soc.* **2023**, *145*, 1194–1205. DOI: 10.1021/jacs.2c10933.
(89) Wang, W.; Gong, J.; Zhao, J.; Zhang, H.; Wen, W.; Zhao, Z.; Li, Y. J.; Wang, J.; Huang, C. Z.; Gao, P. F. Integration of Wallach's Rule into Intermolecular Charge Transfer: A Visual Strategy for Chiral Purification. *Adv. Sci.* **2024**, 2403249.
DOI: 10.1002/advs.202403249.
(90) Cheng, Q.; Hao, A.; Xing, P. Selective chiral dimerization and folding driven by arene–perfluoroarene force. *Chem. Sci.* **2024**, *15*, 618–628. DOI. 10.1039/D3SC05212E.
(91) Storme, K. R.; Schreib, B. S.; Smith, Z. P.; Swager, T. M. Tuning Porosity in Triptycene-Poly(arylene ether)s. *Macromolecules* **2024**, *57*, 7065–7073. DOI: 10.1021/acs.macromol.4c01199.
(92) Martin, R. H. The Helicenes. *Angew. Chem. Int. Ed.* **1974**, *13*, 649–660. DOI: 10.1002/anie.197406491.
(93) Gingras, M. One Hundred Years of Helicene Chemistry. Part 1: Non-Stereoselective Syntheses of Carbohelicenes. *Chem. Soc. Rev.* **2013**, *42*, 968–1006. DOI: 10.1039/C2CS35154D.
(94) Mori, K.; Murase, T.; Fujita, M. One-Step Synthesis of [16]Helicene. *Angew. Chem. Int. Ed.* **2015**, *54*, 6847–6851.
DOI: 10.1002/anie.201502436.
(95) Kiel, G. R.; Patel, S. C.; Smith, P. W.; Levine, D. S.; Tilley, T. D. Expanded Helicenes: A General Synthetic Strategy and Remarkable Supramolecular and Solid-State Behavior. *J. Am. Chem. Soc.* **2017**, *139*, 18456–18459. DOI: 10.1021/jacs.7b10902.
(96) Malik, A. U.; Gan, F.; Shen, C.; Yu, N.; Wang, R.; Crassous, J.; Shu, M.; Qiu, H. Chiral Organic Cages with a Triple-Stranded Helical Structure Derived from Helicene. *J. Am. Chem. Soc.* **2018**, *140*, 2769–2772. DOI: 10.1021/jacs.7b13512.
(97) Wang, Y.; Yin, Z.; Zhu, Y.; Gu, J.; Li, Y.; Wang, J. Hexapole [9]Helicene. *Angew. Chem. Int. Ed.* **2019**, *58*, 587–591.
DOI: 10.1002/anie.201811706.
(98) Jiang, X.; Laffoon, J. D.; Chen, D.; Pérez-Estrada, S.; Danis, A. S.; Rodríguez-López, J.; Garcia-Garibay, M. A.; Zhu, J.; Moore, J. S. Kinetic Control in the Synthesis of a Möbius Tris((ethynyl)[5]helicene) Macrocycle Using Alkyne Metathesis. *J. Am. Chem. Soc.* **2020**, *142*, 6493–6498. DOI: 10.1021/jacs.0c01430.
(99) Xiao, X.; Pedersen, S. K.; Aranda, D.; Yang, J.; Wiscons, R. A.; Pittelkow, M.; Steigerwald, M. L.; Santoro, F.; Schuster, N. J.; Nuckolls, C. Chirality Amplified: Long, Discrete Helicene Nanoribbons. *J. Am. Chem. Soc.* **2021**, *143*, 983–991.
DOI: 10.1021/jacs.0c11260.
(100) Huang, H. C.; Hsieh, Y. C.; Lee, P. L.; Lin, C. C.; Ho, Y. S.; Shao, W. K.; Hsieh, C. T.; Cheng, M. J.; Wu, Y. T. Highly Distorted Multiple Helicenes: Syntheses, Structural Analyses, and Properties. *J. Am. Chem. Soc.* **2023**, *145*, 10304–10313. DOI: 10.1021/jacs.3c01647.
(101) Izquierdo-García, P.; Fernández-García, J. M.; Medina Rivero, S.; Šámal, M.; Rybáček, J.; Bednárová, L.; Ramírez-Barroso, S.;

Ramírez, F. J.; Rodríguez, R.; Perles, J.; et al. Helical Bilayer Nanographenes: Impact of the Helicene Length on the Structural, Electrochemical, Photophysical, and Chiroptical Properties. *J. Am. Chem. Soc.* **2023**, *145*, 11599–11610. DOI: 10.1021/jacs.3c01088.
(102) Shioukhi, I.; Batchu, H.; Schwartz, G.; Minion, L.; Deree, Y.; Bogoslavsky, B.; Shimon, L. J. W.; Wade, J.; Hoffman, R.; Fuchter, M. J.; Markovich, G.; Gidron, O. Helitwistacenes—Combining Lateral and Longitudinal Helicity Results in Solvent-Induced Inversion of Circularly Polarized Light. *Angew. Chem. Int. Ed.* **2024**, *63*, e202319318. DOI: 10.1002/anie.202319318.
(103) Sugiura, H.; Nigorikawa, Y.; Saiki, Y.; Nakamura, K.; Yamaguchi, M. Marked Effect of Aromatic Solvent on Unfolding Rate of Helical Ethynylhelicene Oligomer. *J. Am. Chem. Soc.* **2004**, *126*, 14858–14864. DOI: 10.1021/ja0478882.
(104) Pinar Solé, A.; Klívar, J.; Šámal, M.; Stará, I. G.; Starý, I.; Mendieta-Moreno, J. I.; Ernst, K. H.; Jelínek, P.; Stetsovych, O. On-Surface Synthesis of Helicene Oligomers. *Chem. Eur. J.* **2024**, *30*, e202304127. DOI: 10.1002/chem.202304127.
(105) Gedeon, C.; Del Rio, N.; Furlan, F.; Taddeucci, A.; Vanthuyne, N.; Gregoriou, V. G.; Fuchter, M. J.; Siligardi, G.; Gasparini, N.; Crassous, J.; Chochos, C. L. Rational Design of New Conjugated Polymers with Main Chain Chirality for Efficient Optoelectronic Devices: Carbo[6]Helicene and Indacenodithiophene Copolymers as Model Compounds. *Adv. Mater.* **2024**, *36*, 2314337. DOI: 10.1002/adma.202314337.
(106) Yang, Y.; da Costa, R. C.; Smilgies, D. M.; Campbell, A. J.; Fuchter, M. J. Induction of Circularly Polarized Electroluminescence from an Achiral Light-Emitting Polymer via a Chiral Small-Molecule Dopant. *Adv. Mater.* **2013**, *25*, 2624–2628. DOI: 10.1002/adma.201204961.
(107) Wade, J.; Hilfiker, J. N.; Brandt, J. R.; Liirò-Peluso, L.; Wan, L.; Shi, X.; Salerno, F.; Ryan, S. T. J.; Schöche, S.; Arteaga, O.; Jávorfi, T.; Siligardi, G.; Wang, C.; Amabilino, D. B.; Beton, P. H.; Campbell, A. J. Fuchter, M. J. Natural Optical Activity as the Origin of the Large Chiroptical Properties in π-Conjugated Polymer Thin Films. *Nat. Commun.* **2020**, *11*, 6137–6148. DOI: 10.1038/s41467-020-19951-y.
(108) Rodríguez, R.; Naranjo, C.; Kumar, A.; Matozzo, P.; Das, T. K.; Zhu, Q.; Vanthuyne, N.; Gómez, R.; Naaman, R.; Sánchez, L.; Crassous, J. Mutual Monomer Orientation To Bias the Supramolecular Polymerization of [6]Helicenes and the Resulting Circularly Polarized Light and Spin Filtering Properties. *J. Am. Chem. Soc.* **2022**, *144*, 7709–7719. DOI: 10.1021/jacs.2c00556.
(109) Goedicke, C.; Stegemeyer, H. Resolution and racemization of pentahelicene. *Tetrahedron Lett.* **1970**, *11*, 937–940. DOI: 10.1016/S0040-4039(01)97871-2.
(110) Barroso, J.; Cabellos, J. L.; Pan, S.; Murillo, F.; Zarate, X.; Fernandez-Herrera, M. A.; Merino, G. Revisiting the racemization mechanism of helicenes. *Chem. Commun.* **2018**, *54*, 188–191. DOI: 10.1039/C7CC08191J.
(111) Ravat, P. Carbo[*n*]helicenes Restricted to Enantiomerize: An Insight into the Design Process of Configurationally Stable Functional Chiral PAHs. *Chem. Eur. J.* **2021**, *27*, 3957–3967. DOI: 10.1002/chem.202004488.
(112) Ravat, P.; Hinkelmann, R.; Steinebrunner, D.; Prescimone, A.; Bodoky, I.; Juríček, M. Configurational Stability of [5]Helicenes. *Org. Lett.* **2017**, *19*, 3707–3710. DOI: 10.1021/acs.orglett.7b01461.
(113) Günther, K.; Grabicki, N.; Battistella, B.; Grubert, L.; Dumele, O. An All-Organic Photochemical Magnetic Switch with Bistable Spin States. *J. Am. Chem. Soc.* **2022**, *144*, 8707–8716. DOI: 10.1021/jacs.2c02195.
(114) Vitaku, E.; Dichtel, W. R. Synthesis of 2D Imine-Linked Covalent Organic Frameworks through Formal Transimination Reactions. *J. Am. Chem. Soc.* **2017**, *139*, 12911–12914. DOI: 10.1021/jacs.7b06913.
(115) Sprachmann, J.; Grabicki, N.; Möckel, A.; Maltitz, J.; Monroy, J. R.; Smales, G. J.; Dumele, O. Substituted Benzophenone Imines for COF Synthesis Via Formal Transimination. *Chem. Commun.* **2023**, *59*, 13639–13642. DOI: 10.1039/D3CC03735E.
(116) Xie, Z.; Wang, B.; Yang, Z.; Yang, X.; Yu, X.; Xing, G.; Zhang, Y.; Chen, L. Stable 2D Heteroporous Covalent Organic Frameworks for Efficient Ionic Conduction. *Angew. Chem. Int. Ed.* **2019**, *58*, 15742–15746. DOI: 10.1002/anie.201909554.
(117) Zhong, H.; Wang, M.; Ghorbani-Asl, M.; Zhang, J.; Ly, K. H.; Liao, Z.; Chen, G.; Wei, Y.; Biswal, B. P.; Zschech, E.; Weidinger, I. M.; Krasheninnikov, A. V.; Dong, R.; Feng, X. Boosting the Electrocatalytic Conversion of Nitrogen to Ammonia on Metal-Phthalocyanine-Based Two-Dimensional Conjugated Covalent Organic Frameworks. *J. Am. Chem. Soc.* **2021**, *143*, 19992–20000. DOI: 10.1021/jacs.1c11158.
(118) Sprachmann, J.; Wachsmuth, T.; Bhosale, M.; Burmeister, D.; Smales, G. J.; Schmidt, M.; Kochovski, Z.; Grabicki, N.; Wessling, R.; List-Kratochvil, E. J. W.; Esser, B.; Dumele, O. Antiaromatic Covalent Organic Frameworks Based on Dibenzopentalenes. *J. Am. Chem. Soc.* **2023**, *145*, 2840–2851. DOI: 10.1021/jacs.2c10501.
(119) Jang, M.; Jo, Y.; Oh, I. K.; Jung, H. M.; Lee, S. Suzuki-Miyaura Coupling Reactions Using Phosphite Ligands. *Synthesis* **2009**, *12*, 2073–2075. DOI: 10.1055/s-0029-1216822.
(120) Chen, D.; Xu, G.; Zhou, Q.; Chung, L. W.; Tang, W. Practical and Asymmetric Reductive Coupling of Isoquinolines Templated by Chiral Diborons. *J. Am. Chem. Soc.* **2017**, *139*, 9767–9770. DOI: 10.1021/jacs.7b04256.
(121) Pirkle, W. H.; Finn, J. M.; Schreiner, J. L.; Hamper, B. C. A Widely Useful Chiral Stationary Phase for the High-Performance Liquid Chromatography Separation of Enantiomers. *J. Am. Chem. Soc.* **1981**, *103*, 3964–3966. DOI: 10.1021/ja00403a076.
(122) Flack, H. D.; Shmueli, U. The mean-square Friedel intensity difference in P1 with a centrosymmetric substructure. *Acta Cryst*. **2007**, *63*, 257–265. DOI: 10.1107/S0108767307002802.
(123) Flack, H. D.; Bernardinelli, G. The use of X-ray crystallography to determine absolute configuration. *Chirality* **2008**, *20*, 681–690. DOI: 10.1002/chir.20473.
(124) Jousselin-Oba, T.; Mamada, M.; Wright, K.; Marrot, J.; Adachi, C.; Yassar, A.; Frigoli, M. Synthesis, Aromaticity, and Application of peri-Pentacenopentacene: Localized Representation of Benzenoid Aromatic Compounds. *Angew. Chem. Int. Ed.* **2022**, *61*, e202112794. DOI: 10.1002/anie.202112794.
(125) Pescitelli, G.; Bruhn, T. Good Computational Practice in the Assignment of Absolute Configurations by TDDFT Calculations of ECD Spectra. *Chirality* **2016**, *28*, 466–474. DOI: 10.1002/chir.22600.
(126) Rawat, K. S.; Borgmans, S.; Braeckevelt, T.; Stevens, C. V.; Van Der Voort, P.; Van Speybroeck, V. How the Layer Alignment in Two-Dimensional Nanoporous Covalent Organic Frameworks Impacts Its Electronic Properties. *ACS Appl. Nano Mater.* **2022**, *5*, 14377–14387. DOI: 10.1021/acsanm.2c02647.
(127) Kuroda, R. Crystal and Molecular Structure of [5]helicene: Crystal Packing Modes. *J. Chem. Soc., Perkin Trans. 2.* **1982**, 789–794. DOI: 10.1039/P29820000789.
(128) Schmidt, J. A.; Wolpert, E. H.; Sparrow, G. M.; Johnson, E. R.; Jelfs, K. E. Effect of [n]-Helicene Length on Crystal Packing. *Cryst. Growth Des.* **2023**, *23*, 8909–8917. DOI: 10.1021/acs.cgd.3c00964.
(129) Thommes, M.; Kaneko, K.; Neimark, A. V.; Olivier, J. P.; Rodriguez-Reinoso, F.; Rouquerol, J.; Sing, K. S. W. Physisorption of Gases, with Special Reference to the Evaluation of Surface Area and Pore Size Distribution (IUPAC Technical Report). *Pure Appl. Chem.* **2015**, *87*, 1051–1069. DOI: 10.1515/pac-2014-1117.
(130) Osterrieth, J. W. M.; Rampersad, J.; Madden, D.; Rampal, N.; Skoric, L.; Connolly, B.; Allendorf, M. D.; Stavila, V.; Snider, J. L.; Ameloot, R.; Marreiros, J.; Ania, C.; Azevedo, D.; Vilarrasa-Garcia, E.; Santos, B. F.; Bu, X. H.; Chang, Z.; Bunzen, H.; Champness, N. R.; Griffin, S. L.; Chen, B.; Lin, R. B.; Coasne, B.; Cohen, S.; Moreton, J. C.; Colón, Y. J.; Chen, L.; Clowes, R.; Coudert, F. X.; Cui, Y.; Hou, B.; D'Alessandro, D. M.; Doheny, P. W.; Dincă, M.; Sun, C.; Doonan, C.; Huxley, M. T.; Evans, J. D.; Falcaro, P.; Ricco, R.; Farha, O.; Idrees, K. B.; Islamoglu, T.; Feng, P.; Yang, H.; Forgan, R. S.; Bara, D.; Furukawa, S.; Sanchez, E.; Gascon, J.; Telalović, S.; Ghosh, S. K.; Mukherjee, S.; Hill, M. R.; Sadiq, M. M.; Horcajada, P.; Salcedo-Abraira, P.; Kaneko, K.; Kukobat, R.; Kenvin, J.; Keskin, S.; Kitagawa, S.; Otake, K.; Lively, R. P.; DeWitt, S. J. A.; Llewellyn, P.; Lotsch, B. V.; Emmerling, S. T.; Pütz, A. M.; Martí-Gastaldo, C.; Padial, N. M.; García-Martínez, J.; Linares, N.; Maspoch, D.; Suárez del Pino, J. A.;

Moghadam, P.; Oktavian, R.; Morris, R. E.; Wheatley, P. S.; Navarro, J.; Petit, C.; Danaci, D.; Rosseinsky, M. J.; Katsoulidis, A. P.; Schröder, M.; Han, X.; Yang, S.; Serre, C.; Mouchaham, G.; Sholl, D. S.; Thyagarajan, R.; Siderius, D.; Snurr, R. Q.; Goncalves, R. B.; Telfer, S.; Lee, S. J.; Ting, V. P.; Rowlandson, J. L.; Uemura, T.; Iiyuka, T.; van der Veen, M. A.; Rega, D.; Van Speybroeck, V.; Rogge, S. M. J.; Lamaire, A.; Walton, K. S.; Bingel, L. W.; Wuttke, S.; Andreo, J.; Yaghi, O.; Zhang, B.; Yavuz, C. T.; Nguyen, T. S.; Zamora, F.; Montoro, C.; Zhou, H. C.; Kirchon, A.; Fairen-Jimenez. How Reproducible are Surface Areas Calculated from the BET Equation? *Adv. Mater.* **2022**, *34*, 2201502–2201514. DOI: 10.1002/adma.202201502.
(131) Kandambeth, S.; Mallick, A.; Lukose, B.; Mane, M. V.; Heine, T.; Banerjee, R. Construction of Crystalline 2D Covalent Organic Frameworks with Remarkable Chemical (Acid/Base) Stability via a Combined Reversible and Irreversible Route. *J. Am. Chem. Soc.* **2012**, *134*, 19524–19527. DOI: 10.1021/ja308278w.
(132) DeBlase, C. R.; Silberstein, K. E.; Truong, T. T.; Abruña, H. D.; Dichtel, W. R. β-Ketoenamine-Linked Covalent Organic Frameworks Capable of Pseudocapacitive Energy Storage. *J. Am. Chem. Soc.* **2013**, *135*, 16821–16824. DOI: 10.1021/ja409421d.
(133) Ma, T.; Kapustin, E. A.; Yin, S. X.; Liang, L.; Zhou, Z.; Niu, J.; Li, L. H.; Wang, Y.; Su, J.; Li, J.; Wang, X.; Wang, W. D.; Wang, W.; Sun, J.; Yaghi, O. M. Single-Crystal X-Ray Diffraction Structures of Covalent Organic Frameworks. *Science* **2018**, *361*, 48–52.
DOI: 10.1126/science.aat7679.
(134) Lukose, B.; Kuc, A.; Heine, T. The Structure of Layered Covalent-Organic Frameworks. *Chem. Eur. J.* **2011**, *17*, 2388–2392. DOI: 10.1002/chem.201001290.
(135) Chen, X.; Addicoat, M.; Jin, E.; Xu, H.; Hayashi, T.; Xu, F.; Huang, N.; Irle, S.; Jiang, D. Designed Synthesis of Double-Stage Two-Dimensional Covalent Organic Frameworks. *Sci. Rep.* **2015**, *5*, 14650–14669. DOI: 10.1038/srep14650.
(136) Zhuo, S.; Wang, X.; Li, L.; Yang, S.; Ji, Y. Chiral Carboxyl-Functionalized Covalent Organic Framework for Enantioselective Adsorption of Amino Acids. *ACS Appl. Mater. Interfaces.* **2021**, *13*, 31059–31065.
(137) Zhang, Y.; Položij, M.; Heine, T. Statistical Representation of Stacking Disorder in Layered Covalent Organic Frameworks. *Chem. Mater.* **2022**, *34*, 2376–2381.
(138) Wu, X.; Han, X.; Liu, Y.; Liu, Y.; Cui, Y. Control Interlayer Stacking and Chemical Stability of Two-Dimensional Covalent Organic Frameworks via Steric Tuning. *J. Am. Chem. Soc.* **2018**, *140*, 16124–16133. DOI: 10.1021/jacs.8b08452.
(139) Kang, C.; Zhang, Z.; Wee, V.; Usadi, A. K.; Calabro, D. C.; Baugh, L. S.; Wang, S.; Wang, Y.; Zhao, D. Interlayer Shifting in Two-Dimensional Covalent Organic Frameworks. *J. Am. Chem. Soc.* **2020**, *142*, 12995–13002. DOI: 10.1021/jacs.0c03691.
(140) Emmerling, S. T.; Schuldt, R.; Bette, S.; Yao, L.; Dinnebier, R. E.; Kästner, J.; Lotsch, B. V. Interlayer Interactions as Design Tool for Large-Pore COFs. *J. Am. Chem. Soc.* **2021**, *143*, 15711–15722. DOI: 10.1021/jacs.1c06518.
(141) Kang, C.; Zhang, Z.; Usadi, A. K.; Calabro, D. C.; Baugh, L. S.; Yu, K.; Wang, Y.; Zhao, D. Aggregated Structures of Two-Dimensional Covalent Organic Frameworks. *J. Am. Chem. Soc.* **2022**, *144*, 3192–3199. DOI: 10.1021/jacs.1c12708.
DOI: 10.1021/acs.chemmater.1c04365
(142) Li, Y.; Wu, Q.; Guo, X.; Zhang, M.; Chen, B.; Wei, G.; Li, X.; Li, X.; Li, S.; Ma, L. Laminated self-standing covalent organic framework membrane with uniformly distributed subnanopores for ionic and molecular sieving. *Nat. Commun.* **2020**, *11*, 599.
DOI: 10.1038/s41467-019-14056-7.
(143) Yang, Z.; Chen, H.; Wang, S.; Guo, W.; Wang, T.; Suo, X.; Jiang, D. e.; Zhu, X.; Popovs, I.; Dai, S. Transformation Strategy for Highly Crystalline Covalent Triazine Frameworks: From Staggered AB to Eclipsed AA Stacking. *J. Am. Chem. Soc.* **2020**, *142*, 6856–6860.
DOI: 10.1021/jacs.0c00365.
(144) You, P. Y.; Mo, K. M.; Wang, Y. M.; Gao, Q.; Lin, X. C.; Lin, J. T.; Xie, M.; Wei, R. J.; Ning, G. H.; Li, D. Reversible modulation of interlayer stacking in 2D copper-organic frameworks for tailoring porosity and photocatalytic activity. *Nat. Commun.* **2024**, *15*, 194. DOI: 10.1038/s41467-023-44552-w.
(145) Humphreys, C. The Significance of Bragg's Law in Electron Diffraction and Microscopy, and Bragg's Second Law. *Acta Cryst.* **2013**, *69*, 45–50. DOI: 10.1107/S0108767312047587.
(146) Flanders, N. C.; Kirschner, M. S.; Kim, P.; Fauvell, T. J.; Evans, A. M.; Helweh, W.; Spencer, A. P.; Schaller, R. D.; Dichtel, W. R.; Chen, L. X. Large Exciton Diffusion Coefficients in Two-Dimensional Covalent Organic Frameworks with Different Domain Sizes Revealed by Ultrafast Exciton Dynamics. *J. Am. Chem. Soc.* **2020**, *142*, 14957–14965. DOI: 10.1021/jacs.0c05404.
(147) Wang, W.; Wang, H.; Tang, X.; Huo, J.; Su, Y.; Lu, C.; Zhang, Y.; Xu, H.; Gu, C. Phenothiazine-based covalent organic frameworks with low exciton binding energies for photocatalysis. *Chem. Sci.* **2022**, *13*, 8679–8685. DOI: 10.1039/D2SC02503E.